

Lappeenranta University of Technology
School of Engineering Science
Technical Physics

Yekaterina Rezvova

**MAGNETIC PROPERTIES OF FINEMET ALLOYS DOPED WITH
NIOBIUM**

Examiners: Professor Erkki Lahderanta
D.Sc. Ivan Zakharchuk

ABSTRACT

Lappeenranta University of Technology
School of Engineering Science
Technical Physics

Yekaterina Rezvova

Magnetic properties of FINEMET alloys doped with niobium

2017

59 pages, 35 figures, 1 table.

Examiners: Professor Erkki Lahderanta
D.Sc. Ivan Zakharchuk

Keywords: nanocrystalline soft magnetic materials, FINEMET, magnetic properties

The present Master thesis is devoted to investigation of annealing effects on magnetic properties and microstructure of nanocrystalline FINEMET alloys doped with niobium. Nowadays, the research of new types of soft magnetic materials is a widely discussed topic due to their importance in the field of magnetic devices, such as: EMI filters, magnetic sensors, high frequency power transformers, etc. The thesis is focused on the studies of magnetic characteristics of FINEMET alloys doped with niobium with emphasis on choosing the films with the most suitable parameters for practical application. The research was done by means of SQUID magnetometry, RAMAN spectroscopy, atomic force microscopy and X-ray diffractometry. It was found that annealing at temperature of 450°C lead to the highest level of crystallization Fe_3Si . The films showed very strong uniaxial anisotropy induced by the application of in-plane field during the film deposition process. The obtained good soft magnetic properties of the FINEMET films are well suited for practical applications.

ACKNOWLEDGEMENTS

The work on the Master Thesis has been extensive and exciting. Without support and inspiration from my scientific supervisors, parents and friends, I would not have succeeded.

The work on thesis and related studies were conducted in the research laboratories of LUT (Lappeenranta University of Technology), Lappeenranta, Finland.

I am very grateful to Professor Erkki Lahderanta for the opportunity to conduct research in the university's laboratories and for helping to organize the entire process of studying and evaluating the samples of materials under study.

I am immensely grateful to my supervisor Ivan Zakharchuk for explaining the key points in the study, for his interest and help in any issues related to the creation of my Master Thesis. Thanks you.

I am grateful to Evgeniya Mikhailitsyna from the Institute of Natural Sciences, Ural Federal University, Ekaterinburg, Russia for the provided samples.

I am grateful to Ekaterina Soboleva for assistance in the study of samples on the AFM microscope, for long hours of waiting and help in evaluating the data.

I want to express my gratitude to Anton Komlev and Pavel Geydt for the important support during the whole work.

In conclusion, I want to thank my parents for their faith in my strength. I am thankful also to my close friends for their inspiration and support.

TABLE OF CONTENTS

| | | |
|----------|---|-----------|
| 1 | INTRODUCTION | 7 |
| 1.1 | BACKGROUND..... | 7 |
| 1.2 | OBJECTIVES AND DELIMITATIONS | 8 |
| 1.3 | STRUCTURE OF THE THESIS | 8 |
| 2 | SOFT MAGNETIC MATERIALS | 9 |
| 2.1 | IRON-SILICON ALLOYS | 9 |
| 2.2 | NICKEL-IRON ALLOYS..... | 10 |
| 2.3 | SOFT FERRITES | 10 |
| 2.4 | AMORPHOUS AND NANOCRYSTALLINE MATERIALS | 11 |
| 2.4.1 | NANOCRYSTALLINE SOFT MAGNETIC MATERIALS..... | 12 |
| 3 | MAGNETIC PROPERTIES OF NANOCRYSTALLINE SOFT MAGNETIC MATERIALS | 14 |
| 3.1 | HYSTERESIS | 14 |
| 3.2 | PERMEABILITY | 15 |
| 3.3 | RESISTIVITY | 15 |
| 3.4 | SIZE EFFECT | 16 |
| 3.5 | COERCIVITY | 16 |
| 3.6 | SUPERPARAMAGNETISM | 18 |
| 3.7 | MAGNETIC ANISOTROPIES..... | 19 |
| 4 | EXPERIMENTAL TECHNIQUES | 22 |
| 4.1 | X-RAY DIFFRACTOMETRY | 22 |
| 4.2 | RAMAN SPECTROSCOPY..... | 24 |
| 4.3 | ATOMIC FORCE MICROSCOPY | 26 |
| 4.4 | SQUID MAGNETOMETER..... | 28 |
| 5 | EXPERIMENTAL RESULTS AND DISCUSSION | 32 |

| | | |
|----------|--|-----------|
| 5.1 | FE-CU-NB-SI-B FINEMET SAMPLES | 32 |
| 5.2 | X-RAY DIFFRACTOMETRY RESULTS OF FINEMET ALLOYS | 32 |
| 5.3 | RAMAN SPECTROSCOPY RESULTS OF FINEMET ALLOYS | 36 |
| 5.4 | AFM RESULTS OF FINEMET ALLOYS | 37 |
| 5.5 | SQUID RESULTS OF FINEMET ALLOYS..... | 47 |
| 6 | CONCLUSION..... | 55 |
| | REFERENCES | 56 |

LIST OF SYMBOLS AND ABBREVIATIONS

| | |
|-------|---|
| SQUID | Superconducting Quantum Interference Device |
| AFM | Atomic Force Microscopy |
| XRD | X-ray diffractometry |
| MFM | Magnetic force microscopy |

1 INTRODUCTION

1.1 Background

Historically, a great leap forward to the development and progress of modern society is directly related to scientific discoveries and research in the field of the structure of materials and the availability of useful properties of them that can be applied to various spheres of life. Nanotechnologies in this situation are the key direction that can give mankind a lot of new materials and as a result, the methods of using them. Many properties of solids (melting point, electrical conductivity, transparency region, magnetism, etc.) when decreasing the crystal size to 10 - 20 nm begin to depend on the size [1]. Thus, it becomes possible to create new materials not by changing the chemical composition of the components, but by adjusting the size and shape of the particles of their constituents. Nanocrystals and nanostructures are examples of changes in the properties of substances in a nanoscale state.

Nanocrystalline materials are materials that have a crystal structure with particle sizes (grains) of the order of 5 to 50 nm. The study of the magnetic properties of nanocrystalline materials is of particular interest of the scientific community, in view of the fact that for different methods of fabricating, the same sample can have different magnetic properties. Magnetic properties are characterized by formation and structuring of magnetic domains in the composition of matter. FINEMET alloys form α -Fe(Si) nanocrystals that improve their soft magnetic properties during annealing. Nanocrystalline volume fraction in these alloys is about 80%, and their size is approximately 10 to 12 nm [2-5]. In magnetic studies of nanocrystalline materials, magnetic particles act as a single domain and their behavior is governed by particle size, temperature fluctuations, and can be studied using various methods of investigation. My contribution to this work relates to the study of the magnetic properties and structures of FINEMET alloys. FINEMET alloys are nanocrystalline soft magnetic materials that have good magnetic properties. Investigation of the Finemet alloys structures was carried out using SQUID magnetometry, Raman spectroscopy, AFM microscopy, and X-ray diffractometry. The samples were doped with niobium and had different thicknesses.

1.2 Objectives and delimitations

The purpose of this research work was to measure the magnetic properties of FINEMET alloys doped with niobium. The research process was accompanied by the use of various types of measuring techniques. As a result of the research work, the following issues were revealed:

- Do the samples have magnetic properties?
- How strong are the differences in the characteristics of samples made in different ways?
- Which kind of sample has the best magnetic properties?

1.3 Structure of the thesis

Section 2 contains a description of soft magnetic materials and their characteristics. Section 2 consists of 4 subsections, such as: 2.1 “Iron- Silicon alloys”, 2.2 “Nickel- Iron alloys”, 2.3 “Soft ferrites”, 2.4 “Amorphous and Nanocrystalline materials” and subsection 2.4.1 “Nanocrystalline soft magnetic materials” in which the story of the type of material being examined is described in more detail. Section 3 “Magnetic properties of nanocrystalline soft magnetic materials” contains subsections explaining the magnetic properties of substances, such as: 3.1 “Hysteresis”, 3.2 “Permeability”, 3.3 “Resistivity”, 3.4 “Size effect”, 3.5 “Coercivity”, 3.6 “Superparamagnetism” and 3.7 “Magnetic anisotropies”. Section 4 describes the main research methods. Each subsection corresponds to a certain methodology and tells about the features of the study. Section 4 “Experimental techniques” consists of 4 subsections: 4.1 “X-ray diffractometer”, 4.2 “RAMAN spectroscopy”, 4.3 “Atomic force microscopy”, 4.4 “SQUID magnetometer”. The results of the experiments are described in Section 5. Each subsection 5 of the section provides data on the experiments conducted and the results of the study, such as: 5.1 “Fe-Cu-Nb-Si-B FINEMET samples”, 5.2 “XRD results of FINEMET alloys”, 5.3 “Raman Spectroscopy results of FINEMET alloys”, 5.4 “AFM results of FINEMET alloys”, 5.5 “SQUID magnetometry results of FINEMET alloys”.

2 SOFT MAGNETIC MATERIALS

Soft magnetic materials are materials that can change their magnetic properties, such as domain wall motion and domain magnetization rotation in small field without any obstacles. Their main functions are to change and to reinforce magnetic flux which is produced by an electric current, e.g. in electric transformers. The research of soft magnetic materials includes studies of coercivity, their electrical conductivity and saturation magnetization. Moreover, these materials are characterized by relative permeability which shows the ability of a material to react on small changes of external magnetic field. Soft magnetic materials work in two modes: AC (alternating current) or DC (direct current). In the AC mode, the material will be magnetized alternately from one end to the other during the entire operation, while in the DC mode, the magnetization will occur before the determined task is performed.

Soft magnetic materials can be divided into four groups that will be described below:

- 1) Iron- Silicon alloys
- 2) Nickel- Iron alloys
- 3) Soft ferrites
- 4) Amorphous and Nanocrystalline materials

2.1 Iron- Silicon alloys

“Pure iron” is a main example of soft magnetic materials. However, materials consisting only of pure iron are characterized with very low electrical resistivity. The low resistivity devices are prone to high eddy currents appearing due to changing magnetic field. The eddy currents fade away producing heat, hence, they are considered as direct losses. Following these considerations, it is desirable to increase the resistivity. This task is solved by alloying iron with other materials, for example silicon. The dilution of iron by some additive is capable to reduce the strain-aging which restricts particles from the formation of domain structures. Iron- Silicon alloys are widely known as electrical steel.

Their main application is the core of electric transformer. The main advantages of the Fe-Si alloys are increasing of the electrical resistance of the whole material, decreasing of both magnetostriction and magnetocrystalline anisotropy. However, the addition of large amounts of silicon makes the material brittle and difficult to fabricate. Usually, alloys contain from 3 to 4 wt% of silicon and made in the form of 0.3 - 0.7 mm thick plates.

2.2 Nickel- Iron alloys

One example of soft magnetic properties improvement of iron is alloying iron with nickel. Nickel-Iron alloys are also called Permalloys. A number of Ni-Fe alloys with different magnetic properties are obtained at different doping concentrations of Ni, ranging from 30 to 80 wt%. For example, alloys with high nickel concentration, about 78%, also called Supermalloy, possess high permeability. Alloys containing 65% of nickel have a high sensitivity to magnetic field annealing. Alloys with 50% nickel (Deltamax) have a high saturating magnetization. In alloys with a nickel content of 36%, called Invar, the temperature increase is compensated by volume magnetostriction, thus this alloy has a high magnetic permeability.

2.3 Soft ferrites

General composition soft ferrites are $M\text{Fe}_2\text{O}_3$, where M is a divalent metal. They are used in devices operating with high frequencies instead of metallic soft magnetic materials. Metallic soft magnetic materials are not used in such applications due to high eddy current losses.

Nevertheless, soft ferrites have some disadvantages, such as low magnetic saturation and low Curie temperature. However, among the advantages of soft ferrite over metallic ferrites, the most important are high electrical resistance and high corrosion resistance. The magnetic properties of soft ferrites are specified by the magnetic moments of the metal ions. The ion-ion interaction is antiferromagnetic and leads to a distinctive temperature dependence of the saturation polarization and inverse susceptibility [6 - 7].

2.4 Amorphous and Nanocrystalline materials

In 1967 Duwez and his team noticed a transformation of a material under the

influence of very low temperatures from a liquid state to a nanocrystalline state [8]. These materials began to be called nanocrystalline alloys. Nanocrystalline alloys consist mainly of Fe, Ni, Co, and about 20% of additives, such as boron, carbon, phosphorus and silicon. There are several methods to manufacture the nanocrystalline materials. The most usual manufacturing techniques are planar flow casting (PFL), chill block melt spinning and in-water-quenching technique.

In the PFL, an alloy in a quartz crucible is located close to the surface of a metal drum. Then it is sprayed onto the rotating drum. The chill block melt spinning method is derivative at PFL, and it is suitable for thin films. Both techniques are shown schematically in Fig. 1. In the in-water-quenching technique, soft magnetic films are obtained by the Taylor extraction method. In this case, molten metal is immersed in rotating water. After, using a radio frequency inductor, the metal begins to melt and, by the action of the water flow, a glass capillary is formed, covering the metal core [9].

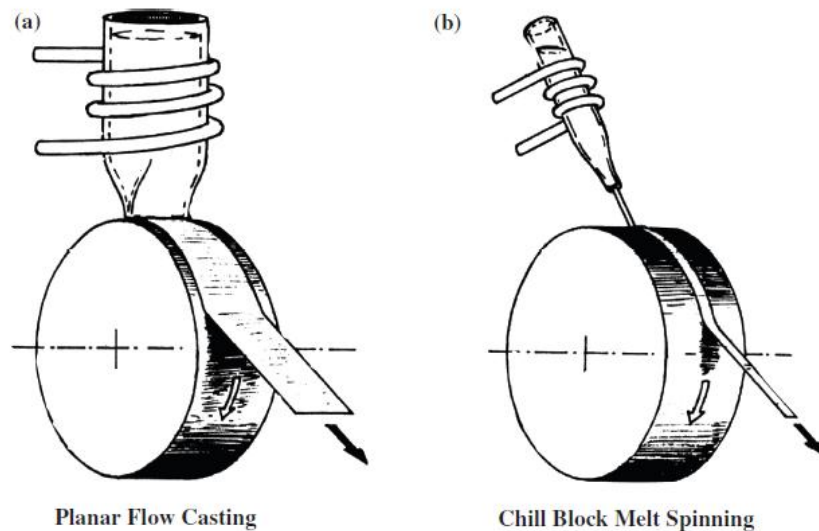


Fig. 1. Preparation of soft magnetic ribbons by means of rapid quenching from the melt by (a) planar flow casting and (b) chill block melt spinning [9].

Recently, the main interest has focused on the study of nanocrystalline materials obtained by annealing. Annealed materials have relatively low anisotropy, high resistivity and good mechanical properties.

2.4.1 Nanocrystalline soft magnetic materials

The first nanocrystalline soft magnetic material was created by the group of researchers from Hitachi Materials Ltd. in 1986. After several years, the results of Yoshizawa, Oguma and Yamauchi were published and the invented material was called FINEMET [2-5]. The abbreviation FINEMET was chosen for these materials due to their “FINE” magnetic characteristics and “METAL” phase structure. FINEMET is unique nanocrystalline soft magnetic material which is based on iron and has excellent magnetic properties [10].

The most important FINEMET consists of combination of Fe-Cu-Nb-Si-B. In this case, silicon and boron are used for constructing an amorphous structure in fast-tempered film. Copper is needed to create clusters that have big concentration of copper on the primary stage of calcination. The reason is that copper clusters act as centers for the beginning of crystallization through the whole volume of material. Niobium forms soften copper clusters and constrain the growth of crystalline phase for increases of temperature. In addition to this, it prevents formation of iron boride [11]. As a result of nanocrystallization, the construction of FINEMET has two stages, such as creation of bcc Fe grains with body-centered cubic lattice (bcc $\text{Fe}_{1-y}\text{Si}_y$) and growing of amorphous surrounding matrix. The size of the grains is about 10 - 12 nm in diameter [12]. For instance, the bcc grains are organized in the DO_3 superlattice structure [13, 14]. The composition of the amorphous matrix is stoichiometric $(\text{Fe}_{1-a}\text{Nb}_a)_2\text{B}$ [15]. Figure 2 shows the schematic of structure of FINEMET.

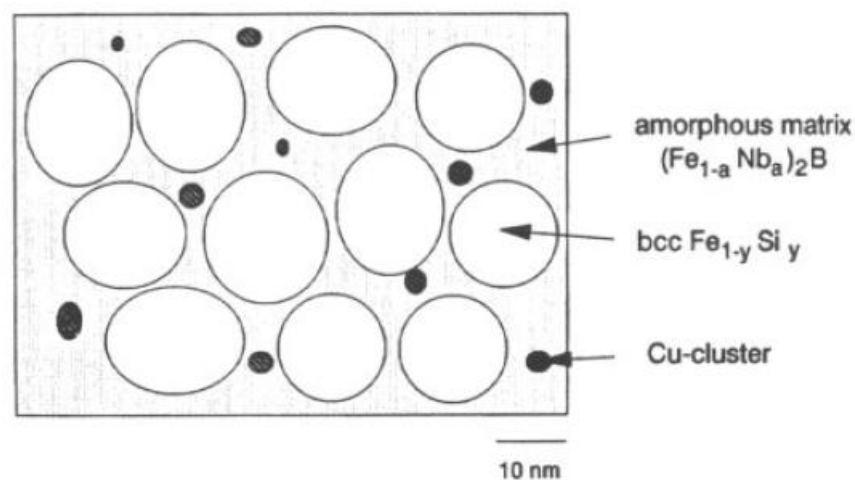


Fig.2. Microstructural characteristics of nanocrystalline FeCuNbSiB (schematic) [1].

Magnetic applications have lack in research of grain sizes. Its aim is to find the solution and make sizes of the grain much smaller than single domain particle and domain wall sizes. However, the main purpose for the industry of soft magnetic engineering is to make the grain size as large as possible. It is needed to reach low coercivities and high permeabilities of the material [16].

3 MAGNETIC PROPERTIES OF NANOCRYSTALLINE SOFT MAGNETIC MATERIALS

In this chapter, the basic magnetic characteristics of nanocrystalline soft magnetic materials are discussed and explained. Nevertheless, the main point of the chapter is to show magnetic properties studies of soft magnetic materials.

3.1 Hysteresis

Hysteresis is one of the important characteristics of magnetic materials, along with coercivity, resistivity and permeability. The hysteresis is a magnetization loop formed as a result of the application of external magnetic field (in steps or continuously) starting from 0 Oe up to H_{\max} , then going to negative field $-H_{\max}$ and back to H_{\max} to close the loop. The form of this loop, depicted in Fig. 3, is associated with the presence of a domain structure in magnetic material. Once the material is magnetized in one direction of magnetic field, the magnetization does not relax to zero after removing the field. Therefore, in order to reduce the remnant magnetization to zero, one needs to apply in opposite direction a field defined as coercivity field. The highest magnetization points in hysteresis loop correspond to the saturation regime (B_s and H_s in Fig. 3), at which the increase in field strength (H) does not lead to an increase in induction (B) [17].

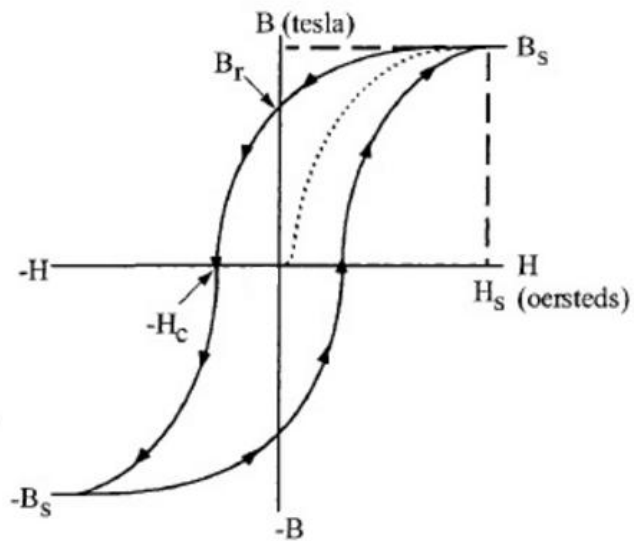


Fig.3. Typical hysteresis loop [17].

3.2 Permeability

If the material has the ability to rapidly magnetize and the ability to conduct a magnetic flux, then it can be said that the material has a magnetic permeability. It represents the dependence of the magnetic flux density on the magnetizing field strengths.

$$\mu = \frac{B}{H}, \quad (1)$$

Permeability can vary in case of changes between the flux density and field strength. The nonlinearity in behavior between B and H leads to differences in ratio of permeability. Figure 4 presents the permeability and maximum of magnetic flux density.

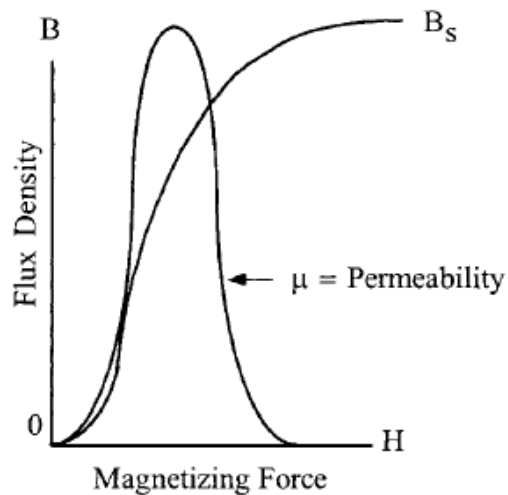


Fig.4. Variation in permeability μ with B and H [18].

3.3 Resistivity

The ability of the material to resist the flow of current is resistivity. There are two types of energy losses in a magnetic material, namely hysteresis losses and eddy current losses. Energy losses during the passage of material through a cyclic state from H to -H and vice versa are called hysteresis losses. They are associated with energy needed to demagnetize material, such as domain wall motion. The loss due to the eddy current occurs when electric currents emerge in the core, thereafter, releasing heat. As a result, high electrical resistance is important characteristic for magnetic materials to obtain low losses.

3.4 Size effect

The main idea of magnetization of nanocrystalline systems is correlation between the structure of crystalline grains and magnetic properties.

The size effect manifests itself as a dependence of material physical properties on the size of specimen. For instance, if we take an iron single-crystal rod that is 1 cm in diameter and compare it to an iron whisker which has 50 nm in diameter on the same densities, so the yield stress in tension will be more for iron whisker. Thus, size effect represents structure-sensitive properties of the specimen.

Magnetic properties have strong dependence on size effect. For instance, the saturation magnetization depends weakly on the size for big specimens. However, the size starts to strongly influence the saturation magnetization when the total number of atoms in whole volume reaches the number of atoms on the surface of specimen. Nevertheless, the coercivity exhibits a very strong size effect without any exceptions.

3.5 Coercivity

The coercivity is one of the most commonly used property for magnetic studies. Furthermore, the coercivity is a theoretical assumption of the magnetic properties of material based on a hysteresis loop. Depending on the application, materials should have high coercivity, e.g. permanent magnets, or as low as possible, e.g. magnetic core of a transformer.

In addition to this, the coercivity of fine particles possesses size effect. Experimentally has been shown that coercivity increases with decrease of the sizes of ferromagnetic fine particles. Further, after increasing until maximum, coersivity begin to decrease to zero value. The relation between coercivity and particle diameter is presented in Fig. 5.

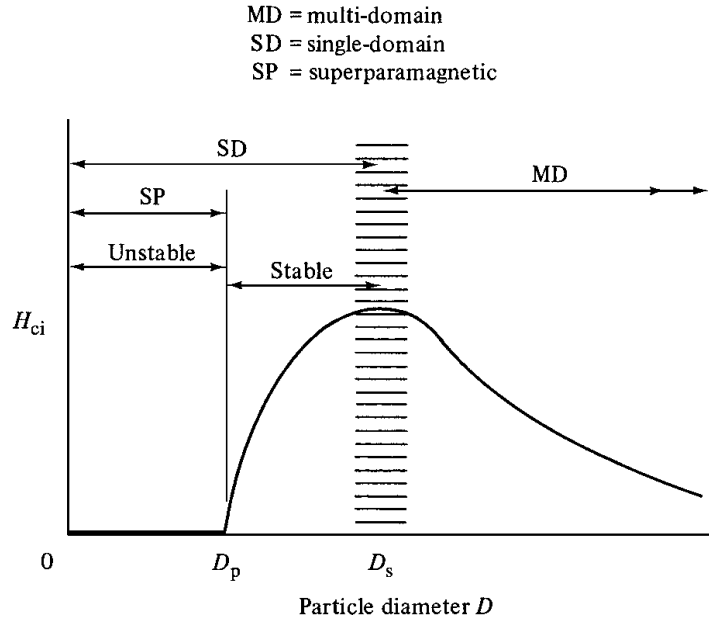


Fig. 5. Variation of intrinsic coercivity H_{ci} with particle diameter D (schematic) [19].

From the figure, three regions of fine particle behavior can be pointed out:

1) Single domain. Particles become single domains when their diameter becomes less than critical. As a result, coercivity reaches its maximum.

2) Multidomain. Domain walls motion change the magnetization of fine particles. Magnetocrystalline energy is determined by the finite width of domain walls. The coercivity and size dependence in general obey the following inverse relationship:

$$H_{ci} = a + \frac{b}{D}, \quad (2)$$

where a and b are constants.

3) Superparamagnetic. Thermal effects influence the particles to be spontaneously demagnetized after reaching zero coercivity. The particle size must be less than critical diameter D_p . These demagnetized particles have superparamagnetic properties [19].

Annealing temperatures influence the structural properties of FINEMET materials, which form the other properties. The coercivity and initial permeability versus annealing temperature dependences are depicted in Fig. 6 with structural characteristics.

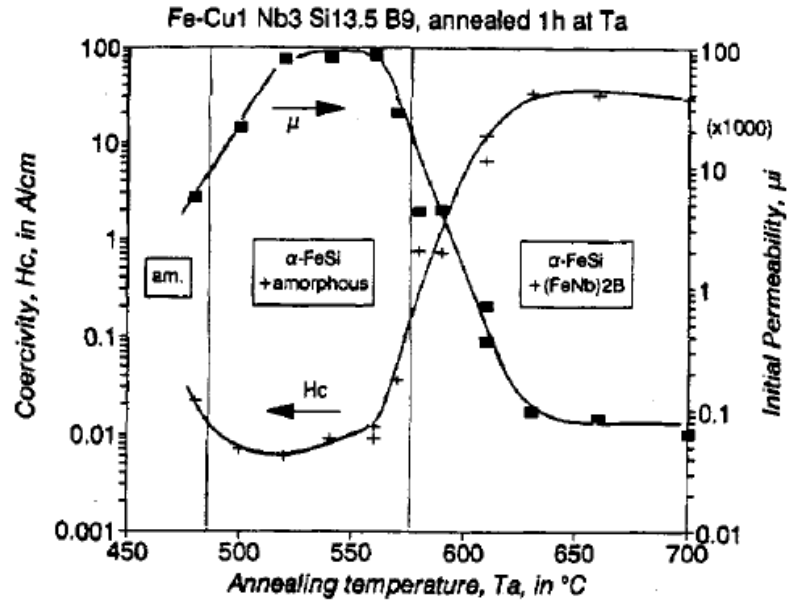


Fig.6. Coercivity, H_c , and initial permeability, μ , of $Fe_{73.5}Cu_1Nb_{30}Si_{13.5}B_9$ as a function of the annealing temperature [15].

Figure 6 represents coercivity and initial permeability of Fe-Cu-NbSi-B. The main point in the analyses of magnetic characteristics is in magnetic anisotropies and ways of their managing. As can be seen from the figure, coercivity and initial permeability have inverse behavior. When one of the characteristics increasing, another is decreasing [15].

3.6 Superparamagnetism

An assembly of individual magnetic moments of the atoms forms one giant total magnetic moment of nanoparticle. When the energy barrier for remagnetization is overcome, and the magnetic moment undergoes temperature fluctuations, as a result, a superspin with a huge moment per particle is created. Superspin is formed as a result of the magnetic coupling of spins within a single-domain particle. This phenomenon is called superparamagnetism.

Superparamagnetism is characterized by a relaxation time, τ . Relaxation time can be expressed by the Neel-Brown equation:

$$\tau = \tau_0 e^{\frac{\delta E}{kT}}, \quad (3)$$

where τ_0 is an attempt time and it is approximately in the range between 10^{-9} and 10^{-12} s;

δE is the height of the energy barrier [20].

In experimental techniques the most interesting is the time of the experiment (t_{exp}), since it affects the value of certain parameters, such as magnetization and blocking temperature. There are two situations which appear when comparing the characteristic time of the experiment (t_{exp}) and the magnetic relaxation time of the material (τ):

- 1) $t_{\text{exp}} \ll \tau$: The experimental time is much smaller than relaxation time. The particles show static behavior of magnetization. In this situation they are in a well defined state, so this can be referred as blocking state.
- 2) $t_{\text{exp}} \gg \tau$: The experimental time is higher than the relaxation time. In this case, due to a diversely directed magnetization, an average fluctuating state is observed. In fact the average value will be measured and this behavior corresponds to superparamagnetic state.

Additionally, exists situation when relaxation time is equal to the duration of experiment ($\tau = t_{\text{exp}}$). In this case, the blocking temperature, T_B , appears between blocking state and superparamagnetic state [20].

3.7 Magnetic anisotropies

Nanoparticles have strict dependence on the direction of magnetic field which they align to. It is generally agreed that nanoparticles have anisotropy. Magnetic anisotropy allows the easy direction of magnetization for spontaneous magnetization. In the case of uniaxial anisotropy, there are two easy directions of magnetization which align opposite directions along the easy axis [20].

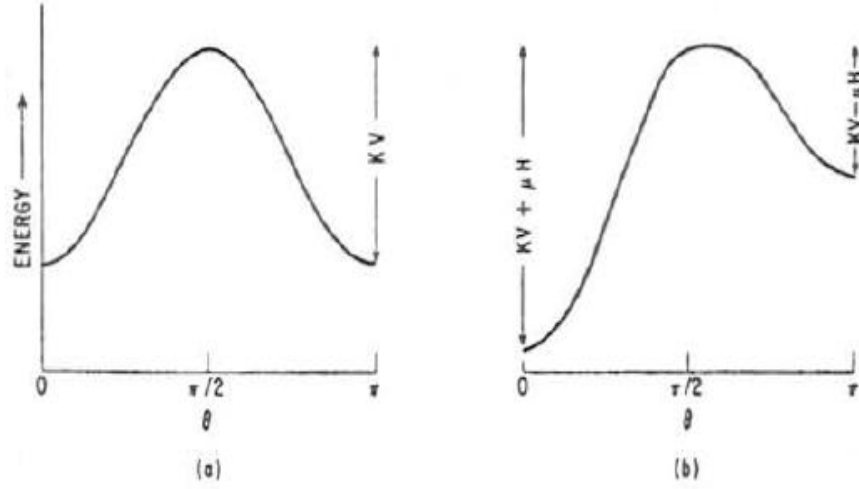


Fig. 7. Dependence of energy of a uniaxial anisotropic particle on the angle between the magnetization and the easy symmetry axis. (a) Without field, (b) with a small field applied along $\theta=0$ [21].

The total energy of a single-domain magnetic grain with uniaxial anisotropy is presented as a combination of magnetic anisotropy and Zeeman energies:

$$E = KV\sin^2(\varphi - \theta) - \mu_0 M_s V H \cos\varphi, \quad (4)$$

where K is uniaxial anisotropy parameter, V is the volume of a grain and M_s is the saturation magnetization. Angle φ shows the dependence between magnetization and magnetic field, although, θ presents the angle between magnetic field and easy direction of magnetization.

The basic anisotropy consists of magneto-crystalline anisotropy, magneto-elastic anisotropy, and magnetic field induced anisotropies [15].

The magneto-crystalline anisotropy originates from crystal symmetry. In fact, crystal axis determines the easy axis magnetization. The magneto-crystalline anisotropy is essentially reduced by small grain size and exchange interaction between the grains [21].

The magneto-elastic anisotropy is based on mechanical stresses (internal or external) due to magnetostrictive coupling. Moreover, Fe-base alloys require large crystalline volume fraction with negative magnetostriction in order to make zero the total

magnetostriction of the FINEMET material. It compensates the high positive magnetostriction value of the amorphous Fe-based matrix [23].

The magnetic field induced anisotropy is a uniaxial anisotropy. In this type of anisotropy, the easy axis is parallel to the direction of the applied field during the manufacturing process. The field annealed samples reveal slightly smaller coercivity than the samples annealed without field. However, despite this, the total anisotropy becomes several times larger [15].

The shape and magnetocrystalline anisotropies affect the magnetic properties of fine particles, in particular, their magnetic hardness. The elimination of one of these components leads to elimination of the dependencies on an anisotropy. For example, material with nearly zero crystalline anisotropy can be constructed with elongated particles or spherical particles which eliminate shape anisotropy. All this is done in order to seal the fine magnetic particles and form a real magnet. An important role has the parameter p , which indicates the volume fraction of the magnetic particles in the assembly. The volume fraction of the particles in the assembly effects on coercivity and depends on type of anisotropy [19].

4 EXPERIMENTAL TECHNIQUES

4.1 X-ray diffractometry

The purpose of the X-ray diffraction analysis is to establish connection between the atomic structure of the studied sample and spatial distribution of the x-ray radiation scattered by a sample. X-ray radiation represents electromagnetic waves with wavelength in the range from 1 nm to 0.001 nm. Atoms and interatomic distances in solid bodies have dispersion of x-ray radiation in the material, so the scattering of X-rays on the substance can be described as diffraction.

Diffraction studies and methods, primarily, the X-ray diffraction experiment are the primary source of information about the structure of matter. Over the past hundred years, Laue's discovery and the subsequent work of Bragg [24] made it possible to formulate theoretical principles of X-ray analysis and make decoding of tens of thousands of structures.

The scattered x-ray radiation from the crystal lattice gives peaks of scattered intensity. Bragg's law determines the direction of these peaks. In Fig. 8 is presented by Bragg's law, where d is the lattice spacing, λ is the wavelength, n is the order of the diffraction maximum, and θ is the diffraction maximum angle (Bragg angle).

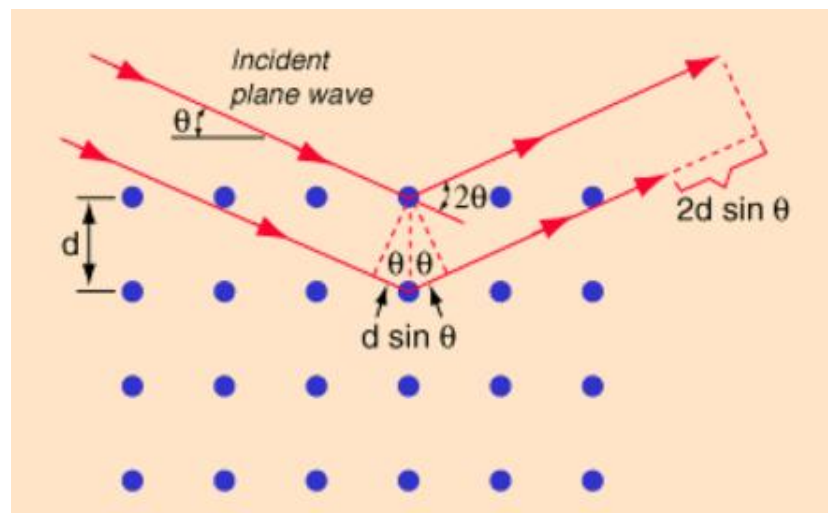


Fig. 8. Bragg's law.

The scattering peaks have the following conditions:

- 1) The angle of incidence = angle of scattering;
- 2) The pathlength difference is equal to an integer number of wavelengths [24].

The diffraction pattern of a single-crystal sample contains information about the size and symmetry of the unit cell, the atomic coordinates, thermal parameters, etc.

X-rays scatter as a result of interaction between X-rays and particles of substance. It occurs because X-rays represent photons of an electromagnetic radiation which have properties of a wave and particle at the same time [25].

X-rays are electromagnetic waves with oscillation frequency of electric and magnetic vectors about 10^{18} Hz. The electric field of X-rays is capable to make the fluctuation of the charged particles with the same frequency. An X-ray beam is created in a vacuum tube by accelerating excited electrons up to several 10 kV. In this case, part of the energy is transformed into heat due to the mobility of the electrons. The remaining part becomes electromagnetic radiation with high penetrating power. This situation leads to formation of photons that have X-ray energy. The process of photon formation occurs by the energy that is obtained when an electron to reach the core levels of atoms (K, L shell). Protons poorly react to fast oscillations of an electric field of X-rays due to their weight. Electrons, being lighter particles, are capable to fluctuate with a frequency of the X-ray photons falling on them ($\sim 10^{18}$ Hz), emitting at the same time X-ray radiation with a frequency of incident wave. Therefore dispersion of X-ray waves happens preferentially for electrons of atoms of material. The intensity of a continuous range of radiation grows in case of increase of tension on X-ray tube. However, there is some feature which is as follows. The line spectrum appears against the background of a continuous range when exist some tension which is strictly determined for each X-ray tube. This line spectrum is called characteristic radiation. Further increase in tension leads to offset of the edge of a continuous range and increase of intensity of continuous and characteristic ranges. Wavelengths of characteristic lines and a mutual ratio of intensity remain invariable. Moreover, wavelengths of characteristic radiations correspond to a series of the maximum values of the radiated frequencies characteristic of anode material. These series designated as K-series and belong to the hardest radiation. The differences between core and outer levels present the emissions with different values, such as $K\alpha_1$, $K\alpha_2$, $K\alpha_3$, etc. The greatest

energy relates to radiation $K\beta$. However, in case of $K\alpha_1$ -radiation quantity of the impulses caught significantly more by the counter of photons. The flows of electrons accelerated between the cathode and the anode of an X-ray tube with a big kinetic energy transfer anode atoms to an excited state, i.e. beat out electrons from internal K-covers of atoms of the anode. Probability for K-shells of the main condition is the greatest. According to selection rules, shell transitions of electrons with external L (α_1 , α_2 – backs doublet radiation) of the main cover, or M (β -radiation) to the vacancy in K-level are followed by removal of an excited state. Transition of atom from initiated in the normal state stimulates an intensive flow of X-ray photons with dominating characteristic of $K\alpha_1$ -radiation. The probability of transitions from M-level is less than from L-level.

The X-ray tube is a source of characteristic radiations with different wavelengths and depends on anode material. Distinctive feature of characteristic x-ray ranges is that they arise on internal electron shells of atoms which have a complete structure. It leads to the fact that ranges of radiation are invariable even if atoms participate in chemical reactions. As a result, ranges of atoms are summarized in the radiographic analysis of structures of the materials consisting of various compounds of atoms. The studied materials in this case unambiguously identified for the structure and concentration of the entering elements.

4.2 RAMAN spectroscopy

Raman effect presents the most noticeable difference from the molecular spectra. The main distinction from the molecular spectra is in the method of absorption of energy quanta by the material and subsequent initiation of rotations and fluctuations in it. In Raman effect, the basic feature is the spectroscopy of scattered radiation [26, 27]. Raman spectroscopy provides information about molecular vibrations, vibrations and low-frequency modes that can be used for sample identification and quantization [28]. This method of spectroscopy was invented by the Indian physicist V. Raman and his team of scientists in 1928 [29]. In 1930 V. Raman won a Nobel prize in the field of inelastic dispersion of light and this effect was called “Raman scattering” [30].

In Raman spectroscopy the dispersion ranges turn out at the radiation of a sample

light with different lengths of waves. Combinational dispersion is a process of inelastic dispersion and interaction between the light and sample. In the course of interaction the Raman range is registered on the basis of scattered radiation. Moreover, it can show the structure of a sample by lines of the turned-out range. These lines contain information about molecular vibrations [26, 27, 30].

The ranges of combinative dispersion can be noticed when monochromatic radiation falls on molecules located perpendicularly in respect to the observer. It occurs in case of agitation by visible or ultraviolet light. Electronic orbitals of molecules displace and fluctuate with a frequency of an exciting light. As a result of it, they become sources of radiation, so-called Rayleigh scattering which has a frequency as an exciting light. At the same time there is energy elimination. All the energy absorbed from primary radiation is given again in the secondary radiation therefore there is no change in amount of energy of a molecule in case of Rayleigh scattering. Electrons at the same time remain in the original configuration space. It occurs because the wavelength of exciting radiation is rather strongly removed from the band of absorption spectra. Thus, the main part of diffused light has the same frequency that exciting light [26, 27, 30].

A big part of diffused light occurs from absorption and secondary emission and has the frequency of the falling radiation. The range of a Raman scattering consists of much more weaker lines relating to lower energy. The appeared lines on lower frequencies are distinguished as Stokes lines, and the anti-Stokes lines correspond to higher frequencies. Stokes lines are noticed in the case of inelastic collision between a photon and a molecule. In this situation the molecule absorbs energy in the amount of one vibration or rotational quantum of energy. The photon loses at the same time the appropriate amount of energy. According to the relation $\Delta E = h \cdot \nu$, frequency depends on value of ν . On the contrary, anti-Stokes lines arise when the molecule is in excited oscillatory or rotational state, and the photon absorbs energy of this oscillatory or rotational quantum so the frequency of a spectral line of combinative dispersion will be one ν more than the frequency of a spectral line of exciting radiation. The molecule is going to the normal state or to the lower exciting state [30].

As the majority of molecules at room temperature are in the oscillatory state, the anti-Stokes lines corresponding to transitions from the higher to lower levels of energy bands have very small probability. Therefore, the typical spectra of combinational

dispersion usually contains, along with Rayleigh, high-intensity Stokes and low-intensity anti-Stokes lines.

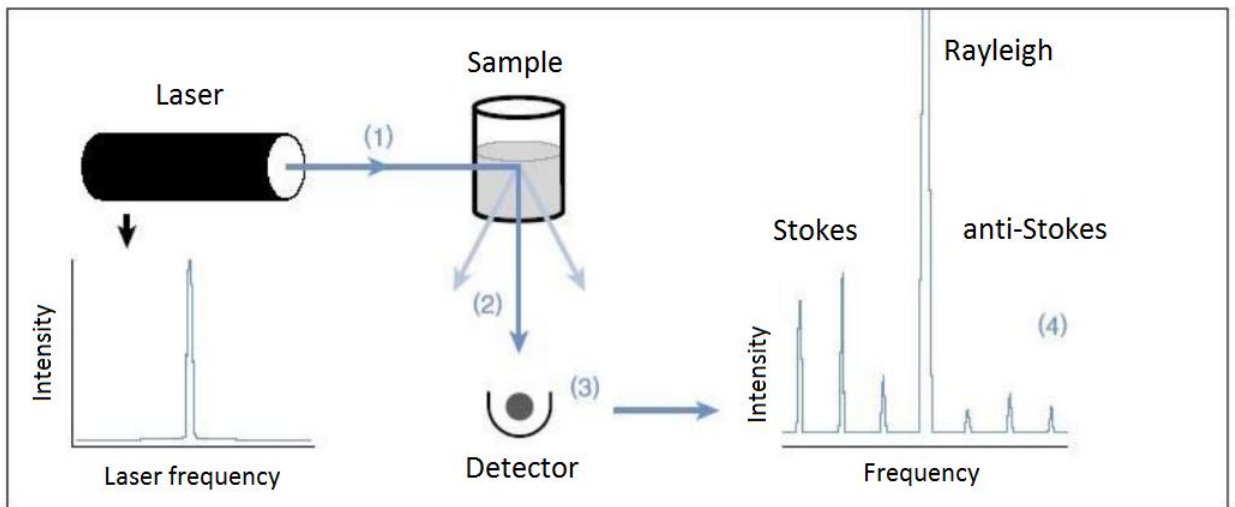


Fig. 9. The principle of Raman spectroscopy [31].

The principle of Raman's work includes four stages (fig. 9). On the first stage laser beam excite the sample. After it goes through the sample the beam scatters in all dimensions (second stage). On the third stage the light partially transiting to the detector. The fourth stage shows the Raman signal through to the detector. The spectra has the primary frequency of light (Rayleigh) and additionally unique spectral features for each sample [31].

4.3 Atomic force microscopy

The Scanning Probe Microscopy (SPM) is one of the modern methods to investigate a solid body surface with high spatial resolution. It allows detecting morphology and local properties of the sample [32].

The atomic force microscope (AFM) was developed in 1986 by G. Binnig, K. Quate, and K. Herber four years after the invention of the scanning tunnel microscope [33].

AFM is a kind of Scanning Probe Microscopy that is based on power interaction between the probe and surface. The principle of AFM work can be explained by Van der Waals interaction between a solid probe tip and the sample surface [34]. These interactions are registered by means of a special probe sensor. The sensor is constructed of an

elastic cantilever with a sharp tip mounted at its end. The tip has a nanodimensional edge. The typical working distance between the tip and sample surface is about 0.1 - 10 nm. When the force is applied to the surface it could lead to bending of the cantilever. Thus, it is possible to receive image of a relief of a surface by registering bend size [35].

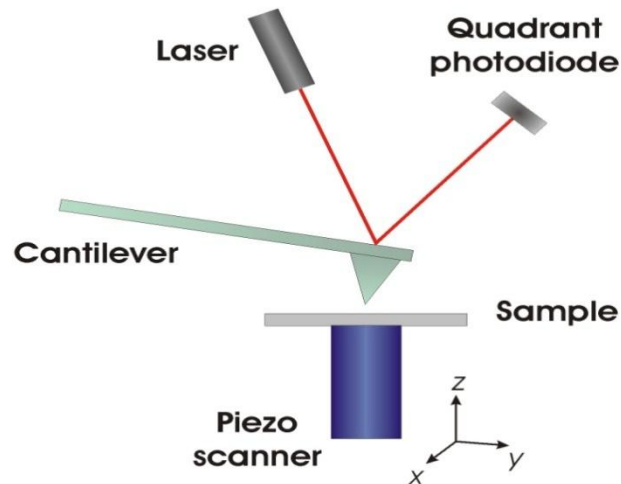


Fig.10. Typical set-up of an AFM

The acquisition of an image using AFM occurs by recording the deviation of the cantilever. Deviations are made by moving the optical lever. The optical lever works when the laser beam hits the cantilever and is reflected. The reflected laser beam falls on a four-segment photodetector. Angular deviations of the cantilever are registered by comparing the positions of the reflected laser beam on a separate segment of the photodetector.

There are three regimes of AFM work: contact mode, non-contact mode, and tapping mode.

To measure the topography of the surface in AFM is used a tapping mode, in which the cantilever slightly touches the contact surface of the sample. The process of determining the topography of the sample and the magnetic properties involves passing the cantilever in a tapping mode in one direction, and “Lift mode” in reverse. In the “Lift mode”, the tip of the probe rises above the surface of the sample to a predetermined distance. Path identical to that passed in a tapping mode close to the surface passes over the surface. In this case, if the probe feels a change in the magnetic forces, then the frequency of the cantilever oscillation changes slightly. The magnetic characteristics of the sample are recorded when passing in the mode of the Lift mode, because in this case the

topography of the sample is practically absent (fig. 11).

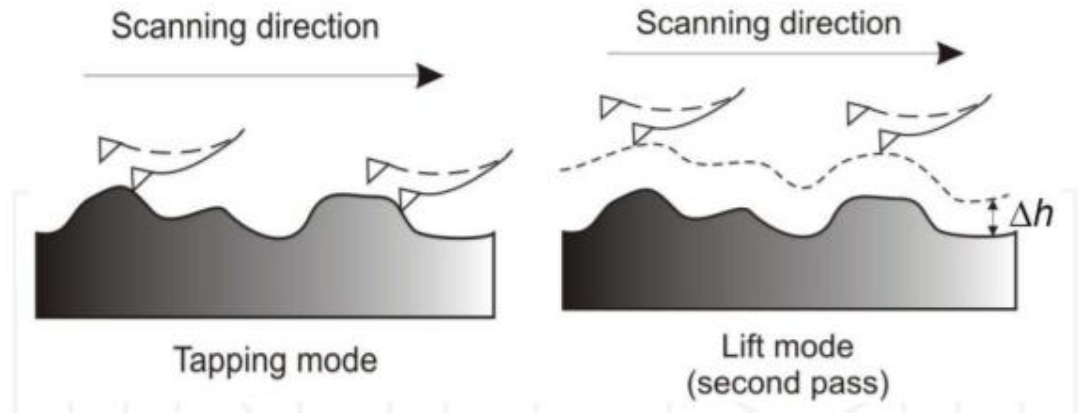


Fig. 11. Outline of the lift mode principle. Magnetic information is recorded during the second pass (right panel). The constant height difference between the two scan lines is the lift height [36].

4.4 SQUID magnetometer

In this section, the working principles of a DC SQUID are discussed. SQUID is a Superconducting Quantum Interference Device [37]. First DC SQUID was invented in 1964 by Robert Jaklevic, John J. Lambe, James Mercereau, and Arnold Silver in Ford Research Labs [3]. The unique function of SQUID is to detect the magnetic flux rather than the changes in levels of the magnetic flux. The DC SQUID combines two superconducting phenomena: flux quantization and Josephson tunneling [38, 39].

Brian Josephson theoretically derived the existence of Josephson Effect in 1961 [40]. He made a research in tunneling between two superconductors and proposed two effects. The first effect showed that direct superconducting current can flow with absence of voltage through the contact between two superconductors. The second effect introduced that alternating superconducting current can flow at a finite voltage. These effects represent Josephson Effect. John Rowell and Philip Anderson at Bell Labs experimentally confirmed its existence in 1963 [41].

In fact, DC SQUID represents a superconducting ring with two Josephson's tunnel contacts. In consideration of the analysis of SQUID an important role is played by wave

properties of electrons. Before forming a uniform stream, the wave of electrons will be divided into two. These waves will tunnel separately and then in the presence or lack of external magnetic field eventually form the general stream. Circulating superconducting magnetic current will be directed due to external magnetic field. However, in lack of external magnetic field no changes will exist [42].

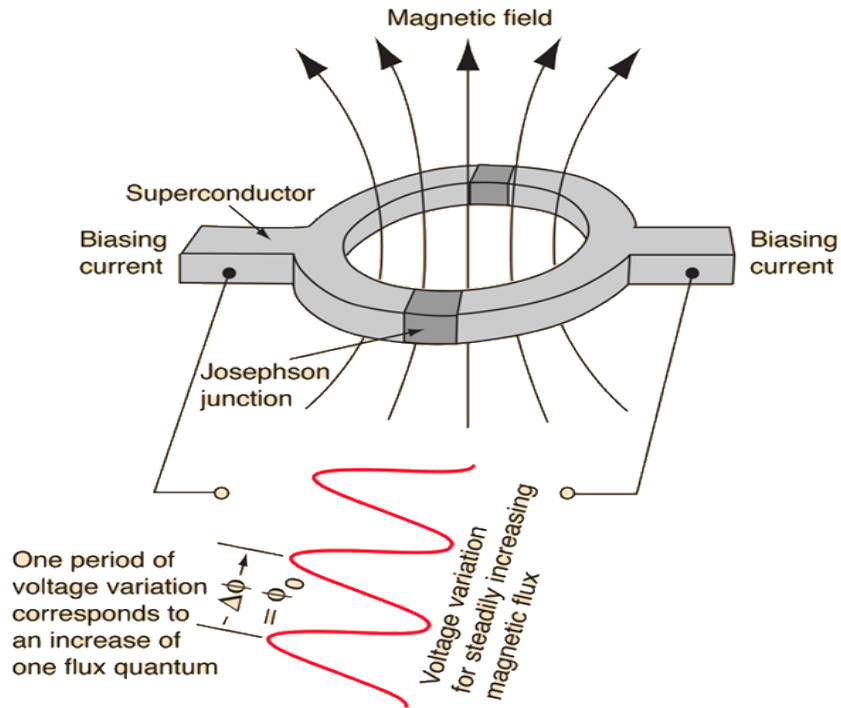


Fig. 12. The SQUID superconducting ring [43].

SQUIDS have high sensitivity to magnetic field because of their strong relation to changes of an external magnetic flux and voltage [44]. It can provide measurements up to 10^{-6} of magnetic flux variations. Basically, there are three components of the magnetometer, namely liquid helium dewar, variable temperature insert and hardware electronics/software to operate the setup and to collect data. The helium dewar comprise the cooling system of the setup, it separates the inner part of the magnetometer from the laboratory environment by vacuum and superinsulation. The inner part presents the insert of SQUID (fig. 13). The most important part of magnetometer is insert, which hold the sample for measuring. Magnetometer's insert consists of a VTI (variable temperature insert), the SQUID detector and a 7 T Magnet. The variable temperature insert basically

consists of sample space with temperature sensors and heaters, SQUIDs, helium level meter, and wiring.

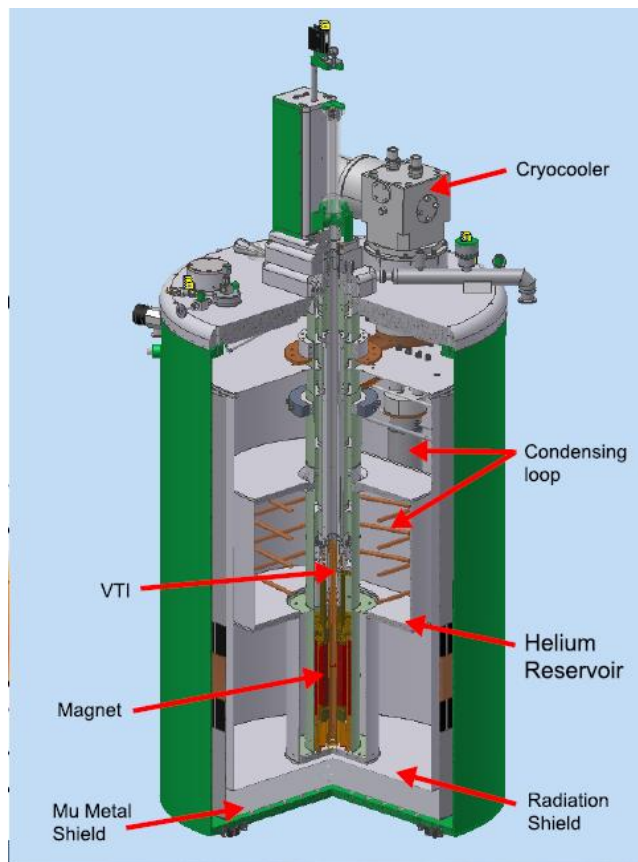


Fig. 13. Three quarter section view of the recondensing cryostat and magnetometer insert [45].

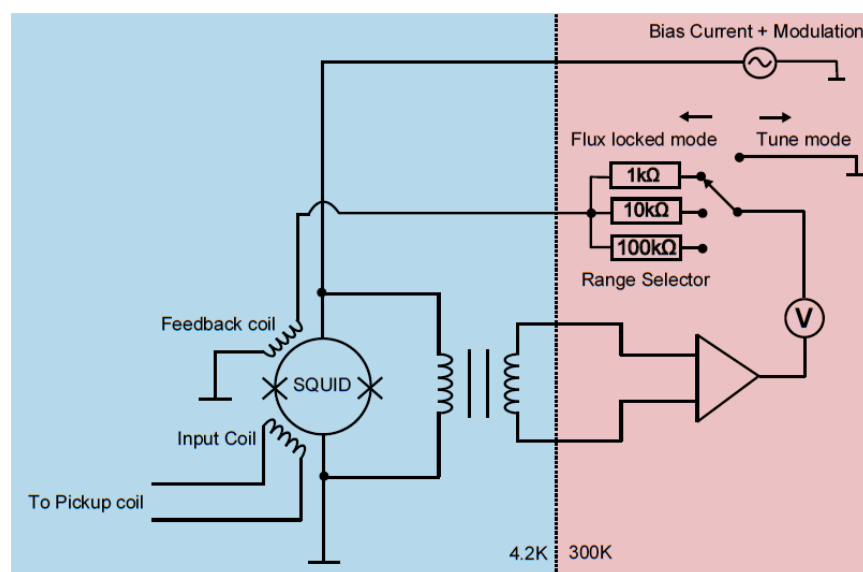


Fig. 14. Schematic diagram showing the operation of the flux detection system [45].

The coil system (fig.14) is used to direct the flux inside SQUID because SQUID does not see the flux directly from the sample. The system of coils contains: Pickup coil, Input coil, Feedback coil. These coils form a magnetic flux transformer. Moreover, the SQUID electronics include an amplifier of an output signal and a circuit of integrated back coupling. This circuit allows setting a magnetic flux in a ring of the interferometer which compensates change of an external magnetic flux. The dependence of the voltage of interferometer from the outside magnetic field is called the signal characteristic. The signal on an output of the SQUID represents a signal of a circuit of back coupling which is proportional to change of an external magnetic flux [44].

5 EXPERIMENTAL RESULTS AND DISCUSSION

5.1 Fe-Cu-Nb-Si-B FINEMET samples

In this thesis, FeCuNbSiB thin films comprising a FINEMET alloy were used. The films were processed by using a radio frequency (RF) sputtering technique. A series of samples with thickness varying from 10 to 200 nm were prepared. The films were deposited on Corning glass substrates from $\text{Fe}_{72.5}\text{Cu}_{1.1}\text{Nb}_2\text{Mo}_{1.5}\text{Si}_{14.2}\text{B}_{8.7}$ targets. The deposition was performed in argon atmosphere with process pressure of 10^{-3} Torr after the base pressure in the chamber had achieved $1 - 2 \cdot 10^{-6}$ Torr. In order to induce uniaxial magnetic anisotropy, which is important in practical applications, the film depositions and thermal annealing were done in in-plane external magnetic field of 100 Oe. The samples were annealed in the sputtering chamber at 350 °C, 400 °C, and 450 °C for 30 minutes under the sputtering conditions (Ar atmosphere, working pressure of 10^{-3} Torr and in-plane magnetic field of 100 Oe). The film thicknesses were determined by the deposition rate and verified using a Dektak150 stylus profilometer. Thicknesses were found to be 10, 30, 50, 100, and 200 nm.

5.2 X-ray diffractometry results of FINEMET alloys.

The investigation of the structure of the FINEMET samples was done by X-ray diffractometry. The diffraction pattern is formed by the interaction of X-rays with the studied material. In this interaction, X-rays are scattered from the atoms of the material. The size and shape of the material particle affect the intensity of the diffraction of the outgoing waves and also their direction [46].

The measurements were carried out using the Bruker D8 Advance X-Ray diffractometer. The work of the diffractometer Bruker D8 ADVANCE is based on the interaction of the anode Cu $K\alpha$ and X-rays. In a high-voltage field, a directional beam of electrons generates X-rays that have sufficient energy to penetrate the target.

Information on the properties of the measured samples is realized by a diffractometer using data collection in the directions 2Theta and Gamma. The 2Theta direction was used in the present research.

The diffractometer was configured to measure at a voltage of 40 kV and a current of 40 mA, secondary monochromator with Cu-K α radiation ($\lambda = 1.5418 \text{ \AA}$). Samples were cut in $3 \times 5 \text{ mm}^2$ size for X-ray powder diffraction and magnetic measurements.

At the same time, diffraction patterns were obtained at 2Theta every 0.05° . Measurements were made in the angular range from 10° to 90° in steps of 0.05° . The time for one step was 0.5 second. The whole process of measuring of one sample took 20 minutes.

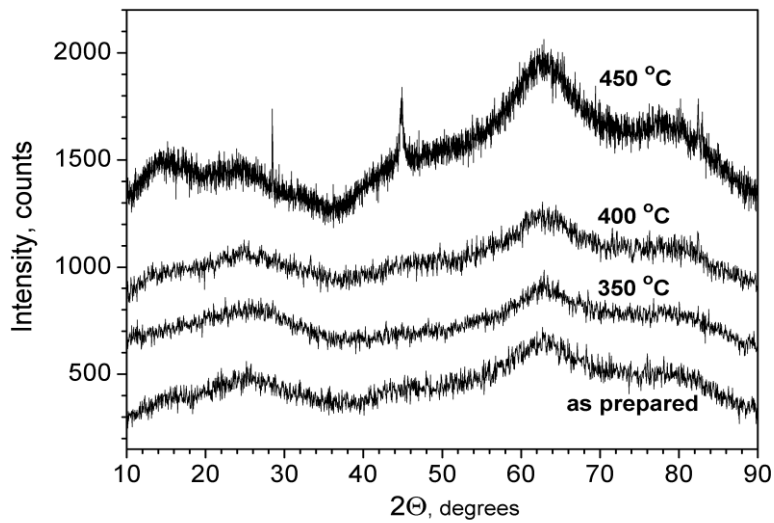


Fig.15. The results of measurement of prepared samples of FINEMET alloy doped with niobium without annealing and annealed at different temperatures ranging from 350°C to 450°C .

The investigation was carried out on four samples prepared at different annealing temperatures and without annealing. The results are shown in fig. 15. The first X-ray diffraction result of the FINEMET alloy without annealing at shows that throughout the entire measurement, the intensity of scattering ranged from 200 counts to 600 counts with a scatter of values corresponding to approximately 100 counts. At the same time, the intensity peak is 700 counts, which corresponds to 63° 2Theta measurement. Next, was considered the sample that was annealed at 350° . It should be noted that the pattern of variations in the intensity dependence on the measurement angle was similar to the previous sample in form, but differed in intensity values. During the measurements, the

peak was also marked at 63° 2Theta, but with an intensity value of 980 counts. The third sample was annealed at 400° . It showed maximum value at an intensity of 1300 counts at 63° 2Theta. The fourth sample was annealed at 450° and presented the greatest interest in studies, since it showed two additional peak spikes at 28° and 45° at 2Theta. The main peak corresponds to 63° 2Theta, with a maximum intensity of 2050 counts. In addition, the obtained measurement pattern was similar in form as the previously studied samples. However, an interesting aspect of the measurements is a peak with an intensity of 1850 counts at 2Theta equal to 45° , which corresponds to crystallites of Fe_3Si .

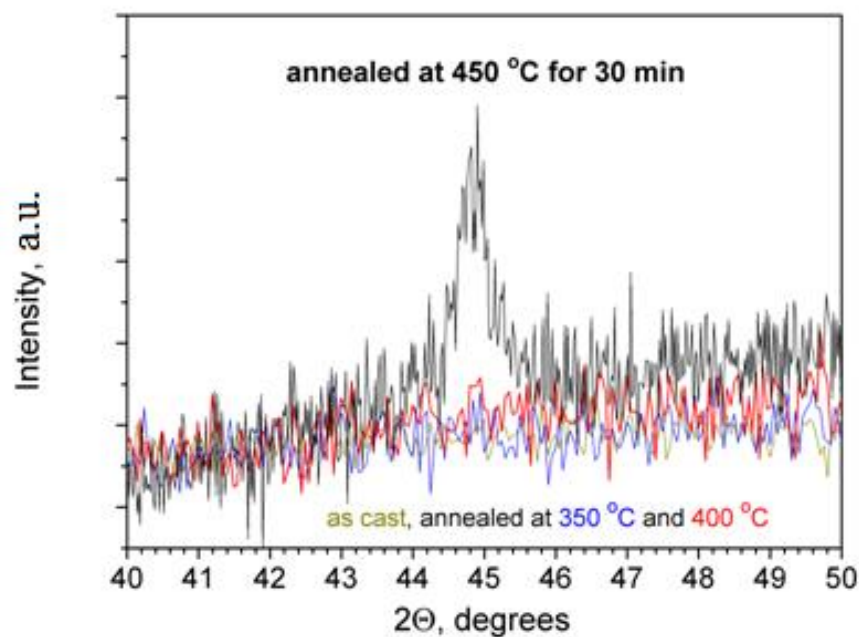


Fig. 16. The measurement data of the test samples in the range from 40° to 50° degrees 2Theta.

The spectra in fig.16 shows of the background signal produced by the sample holder and information about the studied materials. This graph represents four curves that are indicative of the presence of structural features in FINEMET alloys. In the first experiment, an additional peak was observed at approximately 45° from a sample annealed at 450° for 30 minutes. This peak is also seen at 45° when the experiment is repeated in the range from 40° - 50° 2Theta measurement. The peak at 45° shows that the sample prepared at the highest annealing temperature crystallizes in Fe_3Si . The remaining samples prepared without annealing and at annealing temperatures of 350°C and 400°C , have an amorphous structure and did not crystallize.

The X-ray diffractometry is a rather convenient method for studies of sizes of crystallites constituting materials. It is known that crystalline structures with X-ray analysis show characteristic of diffraction peaks. The broadening of the peaks is due to the imperfect crystallinity of the structure of the material being studied. The size of the crystallite is the size of the diffractive domain and it may not coincide with the particle size of the material. Paul Scherrer noted the relationship between the dimensions of the crystallites and the width of the peaks. An equation to calculate the average dimensions of the crystals was deduced in 1981 by Paul Scherrer [47]. This equation is based on the relationship between the width of the diffraction peak and the crystallite size:

$$L = \frac{K \cdot \lambda}{\beta \cdot \cos \theta}, \quad (5)$$

where λ is the X-ray wavelength, β is full width at half maximum (FWHM) measured in radians, θ is the half of angle of 2θ that reflected from crystalline plane, K is the Sherrer constant dependent on crystallite's shape. For spherical shape of the crystallite K value is 0.9 [46, 47].

To calculate the crystallite size of the narrowed peak it is needed to use the Sherrer's equation. In order to use the equation and to find the size of Fe_3Si crystallites, the values of parameters of the Fe_3Si peak were extracted from the XRD data: $K=0.9$, $\lambda=1.5418 \text{ \AA}$, $2\theta=45^\circ$, so the half of angle is $\theta=22.5^\circ$. For calculation of the β parameter it is needed to find the FWHM. FWHM presents the difference between the two positions on the 2θ scale of the middle part of the intensity peak. In our case, these positions are 45.17° and 44.7° . The FWHM should be taken in radians for Sherrer equation, so:

$$\beta = (45.17 - 44.7) \cdot 3.14 \div 180 = 0.0082(\text{rad})$$

Having all the parameters of the studied structure, it is possible to calculate the average crystallite size, as:

$$L = \frac{0.9 \cdot 1.5418}{0.0082 \cdot \cos 22.5} = 169 \text{ \AA}$$

As the result of calculation we found the size of Fe_3Si crystallite, which is equal to 169 \AA or 16.9 nm . Such value in general conforms with the size of the huge amount of smallest particles found on the AFM topography maps.

5.3 Raman Spectroscopy results of FINEMET alloys.

The measurements of molecule vibrational and rotational properties of the FINEMET alloys were obtained by Raman spectroscopy in order to inspect the composition of studied materials. Here we investigated whether there are any traces of magnetic components on the surface of FINEMET alloys. The experiment was made by micro-Raman setup Horiba Jobin Yvon LabRAM 300 Spectrometer. This Spectrometer is designed for Raman measurements with different forms of spectral resolution.

Raman spectroscopy studies the low-frequency modes, which are correlated with the processes of transitions in the molecular system of the sample. The basis of Raman spectroscopy is Raman scattering. Lasers are used to provide information of low-frequency modes in the process of interaction between the sample and laser light. The behavior of the laser beam in sample leads to shift of the energy of the inelastically scattered photons due to a change of their wavelengths. As a consequence, one obtains a Raman spectrum that records inelastically scattered photon data, such as intensity and frequency. The use of Raman scattering is effective when studying and identifying the composition of the samples, since each sample has a unique Raman spectrum.

Raman spectroscopy measurements were carried out in the backscattering geometry. Spectrometer obtains He-Ne laser light source of 632.8 nm. The spectra were excited with power density $\sim 10^4$ W/cm². For focusing of the laser beam and collecting scattered light was used a 100× microscope objective. In the study, samples with a film thickness of 30 nm, 50 nm and 100 nm were used. Unfortunately, the samples of FINEMET 30 nm and 50 nm thick were burned under the laser beam, so that exact data could not be obtained. For the 100 nm thick sample was used a filter which decreased the intensity of the laser in $10^{0.3}$ times. This made it possible to obtain data about the structural features on the sample surface. After the experiment the surface was checked for traces of burns and no visible changes were observed. The investigation was done with sample annealed at 400°C.

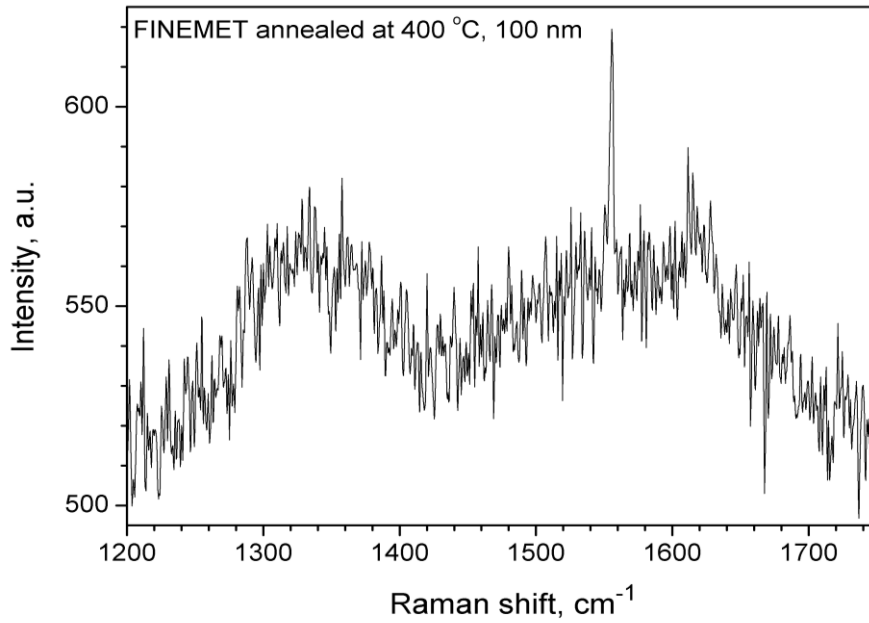


Fig. 17. Raman spectra for FINEMET thin film with thickness 100 nm and annealed at 400°C.

As can be seen from Fig. 17, in to Raman spectroscopy was observed a double maximum in the range from 1300-1600 cm^{-1} . The intensities for both peaks are practically equivalent. However, there is one additional peak spike at 1560 cm^{-1} of Raman Shift. This peak can be referred to the peak of polycrystalline graphite at 1600 cm^{-1} . Also, it should be noted that the peak of 1300 cm^{-1} refers to disordered defective graphite [50].

The origin of the peak at 1600 cm^{-1} does not refer to the internal composition of the sample, since the composition does not contain a graphitic carbon. As for the presence of the graphitic carbon, it is caused by possible surface contamination of the sample, although preliminary measures have been taken on clean surface.

5.4 AFM results of FINEMET alloys.

Measurements of samples of FINEMET thin films were performed in the regime of Magnetic Force Microscopy (MFM) by means of an atomic-force microscope.

Magnetic Force Microscopy can detect the presence of magnetic domains in the

structure of the material close to its surface. The presence of magnetostatic interactions and variations of the magnetic field makes it possible to conclude that the material is magnetized and to analyze the location of the domain agglomerations in the material, as well as their size.

Magnetic Force Microscopy is realized via combination of two different modes, such as Tapping mode and Lift mode. During the experiment was used a magnetic probe MESP-RC, consisting of cobalt and chromium. This probe has a spring constant equal to 5 N/m, which is the stiffness of the probe [51]. The radius of MESP-RC probe is 40 nm [50]. The velocity at which the probe scanned the sample was 3 $\mu\text{m}/\text{sec}$. All measurements were taken at a resolution of 512x256 pixels.

By means of the AFM, a series of Fe-Cu-Nb-Si-B FINEMET alloy samples having different thicknesses and annealed at 450°C were investigated. The first sample that was taken for research had a thickness of 10 nm. The measurements were carried out at the lift distance of 50 nm, which was sufficient to obtain a magnetic map of the sample surface. An optical photo of the sample surface before the experiment is shown in Fig. 18.

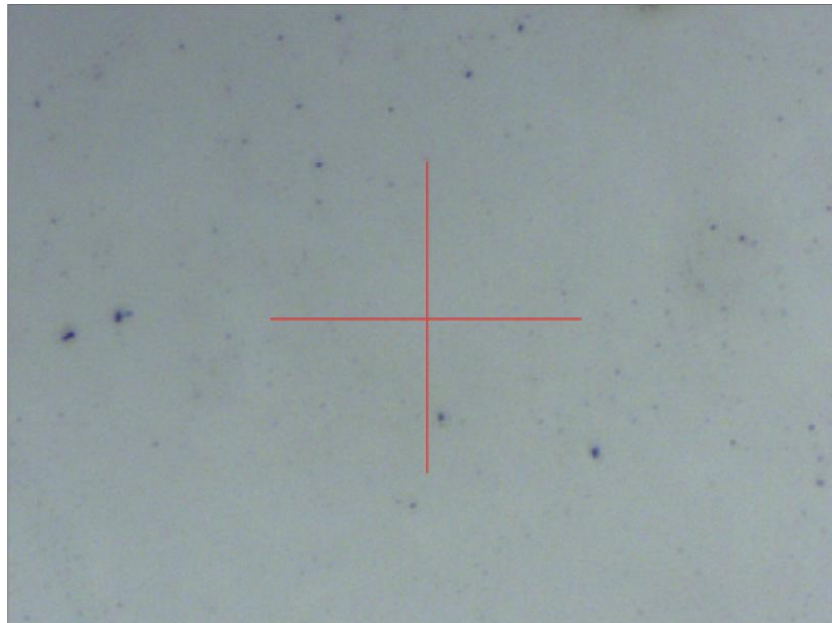


Fig. 18. Optical view of the scanning area of FINEMET sample with thickness 10 nm.

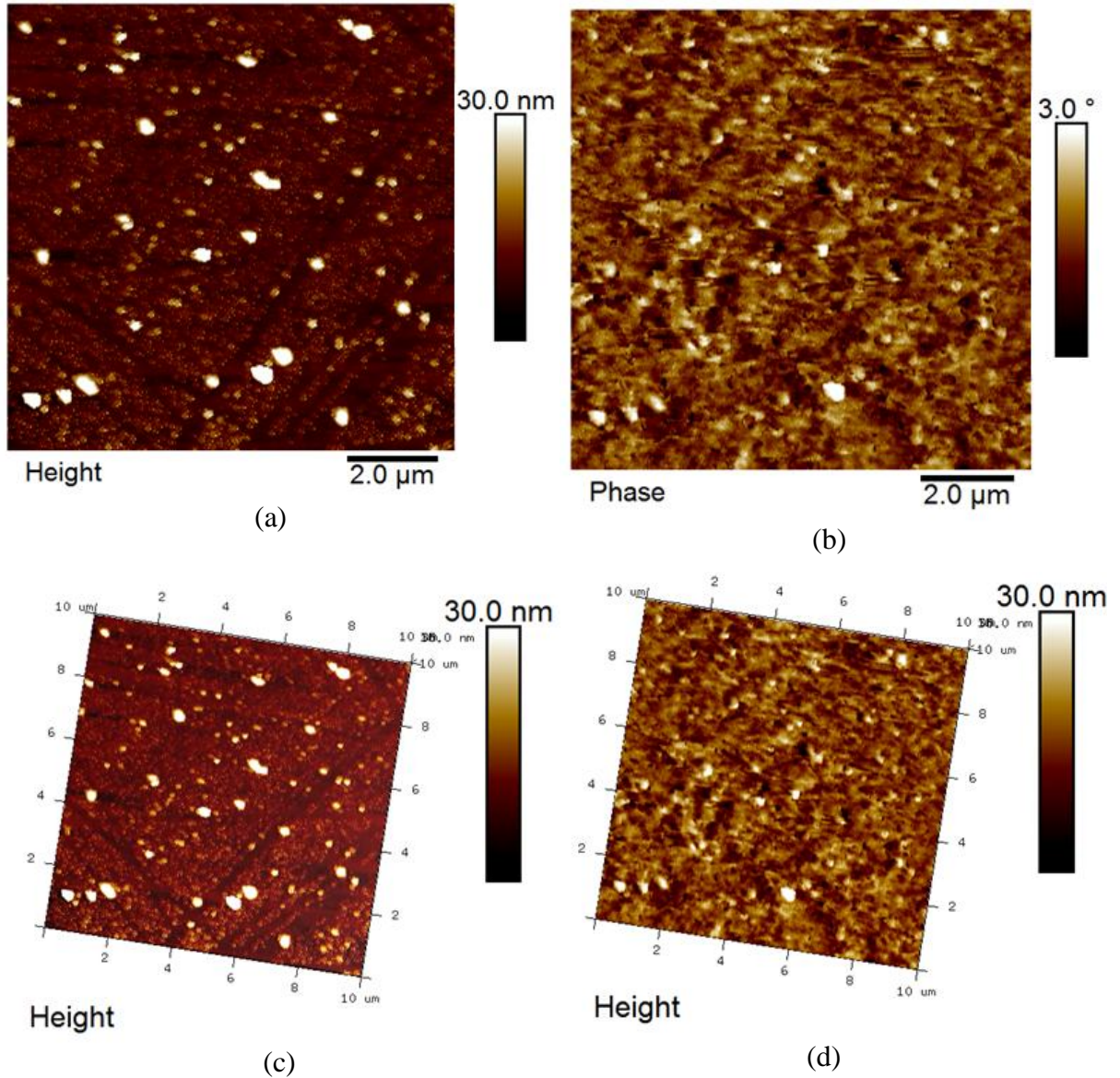


Fig. 19. FINEMET thin film with thickness of 10 nm a) 2D topography, b) 2D magnetic map, c) 3D topography in real scales, d) 3D phase MFM map overlaid on topography.

The investigated area of 10 μm by 10 μm of the FINEMET sample had a root mean square (RMS) roughness of 4.4 nm and an average roughness of 2.3 nm. The topography of the sample surface reflects the presence of different particle sizes on its surface. In this case, 20 large particles, 35 medium sized particles and many small particles were detected. However, it is not possible to calculate the number and characteristics of small particles, in the case of their huge number. Nevertheless, the average height of large particles was 27 nm with an average diameter of 300 nm. As for particles of medium size, the average

height was 15 nm at a diameter of 150 nm.

From the data it can be seen the presence of a magnetic relief in a sample that differs from the topography of the surface. In this case, the magnetic relief is indicated in Fig. 19 (b) as dark dots (domains) over the entire surface of the sample which does not repeat the topography and are not connected with it. The typical size of the contrast of the oppositely oriented domains is approximately 0.3° of phase shift in the MFM channel. Also domains with a contrast of 0.6° to 0.8° were identified using the analysis in the NanoScope Analysis 1.8 software. The width of the oppositely oriented domains was 300-400 nm.

The second examined sample was FINEMET film with a thickness of 30 nm. The optical image of the investigated region of the sample is shown in Fig. 20.

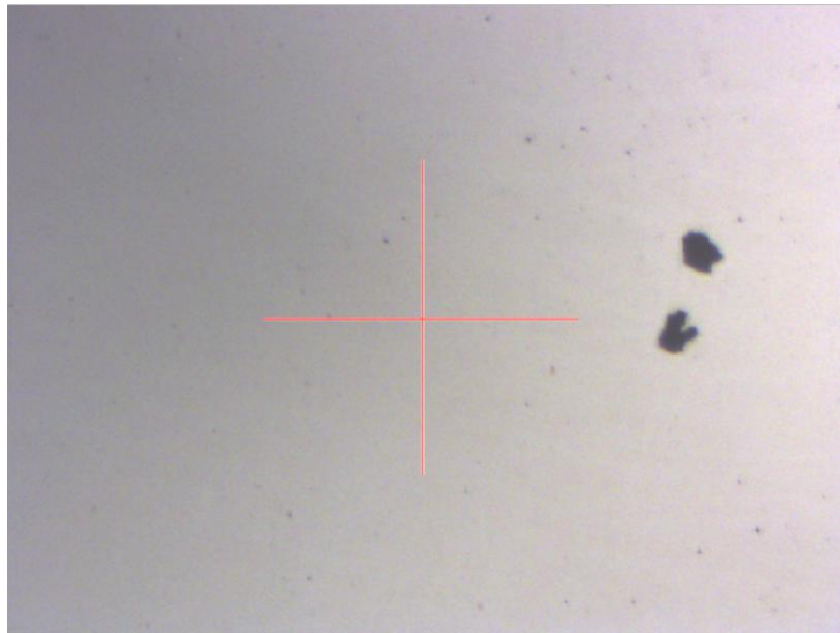


Fig.20. Optical view scanning area of FINEMET sample with thickness 30 nm.

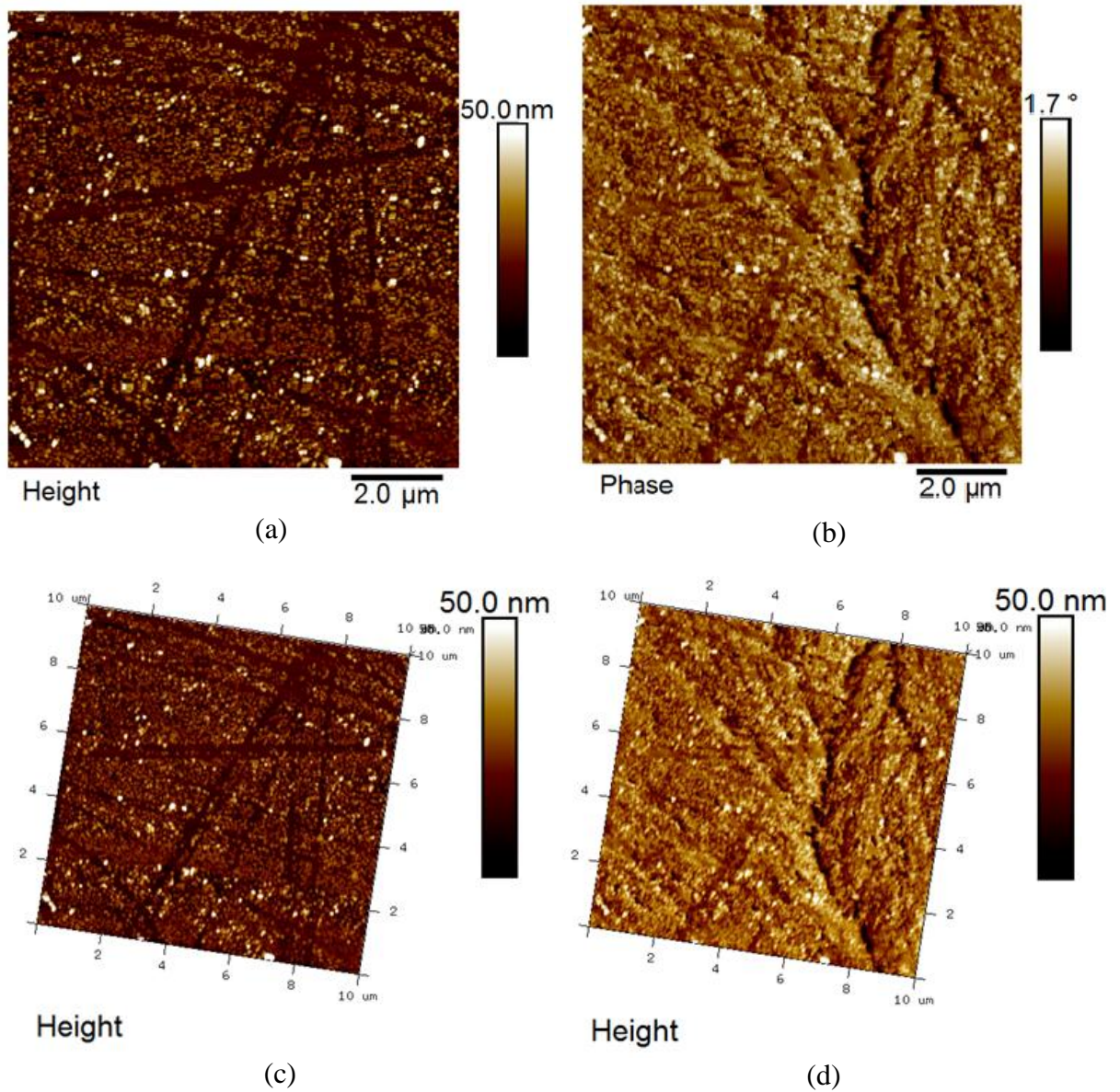


Fig. 21. AFM pictures of FINEMET thin film with thickness of 30 nm a) 2D topography, b) 2D magnetic map, c) 3D topography in real scales, d) 3D phase MFM map overlaid on topography.

In the sample with thickness 30 nm, the surface relief is non-uniform and has an RMS roughness of 6.9 nm and an average roughness of 5.4 nm. At the same time, there were found particles of medium and small size. Particles of medium size have a diameter of 140 - 200 nm with a height of 40 nm. Particles of small size fill the main space of the investigated region $10 \mu\text{m} * 10 \mu\text{m}$. The magnetic map of the film shows the presence of a domain structure in the sample that does not depend on its topography, however sometimes it repeats the scratches on the surface of the sample. According to this, it is worthwhile to

pay attention to the contrast of the opposite oriented domains, which is 1° of phase shift in the MFM while the normal contrast value is 0.2° of the probe phase shift in the MFM. This contrast is revealed for domains with a width of 300-600 nm.

The third studied sample was a thin Fe-Cu-Nb-Si-B FINEMET film with thickness of 50 nm. The type of the investigated area is shown in Fig. 22. The topography of the sample surface in 2D is presented in Fig. 23 (a) and 3D in Fig. 23 (c). In addition to this, the magnetic map is presented in the 2D in Fig. 23 (b). Moreover, the full picture in the 3D dimension is shown in Fig. 23 (d), which consists of magnetic map superimposed over the topography in real scales.

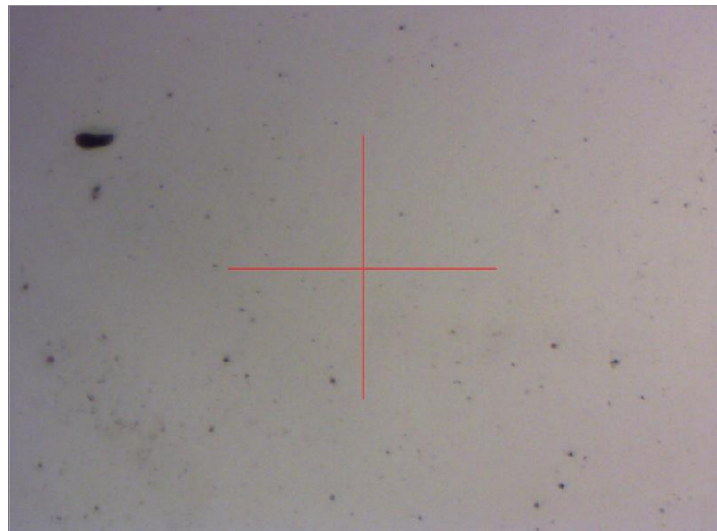
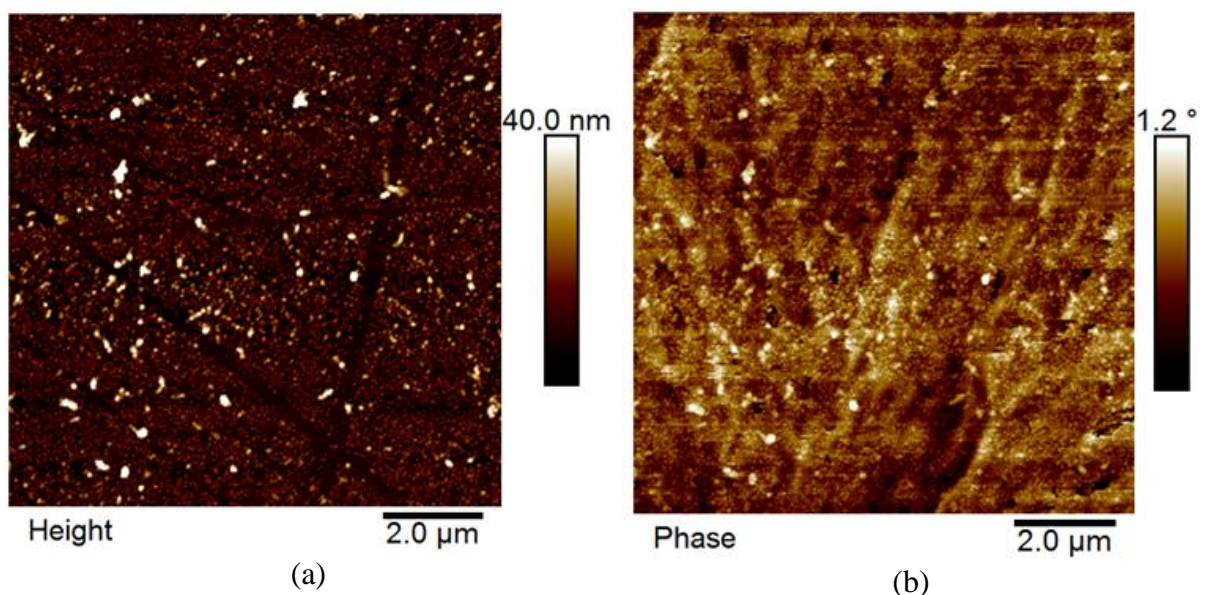


Fig.22. Optical view scanning area of FINEMET sample with thickness 50 nm.



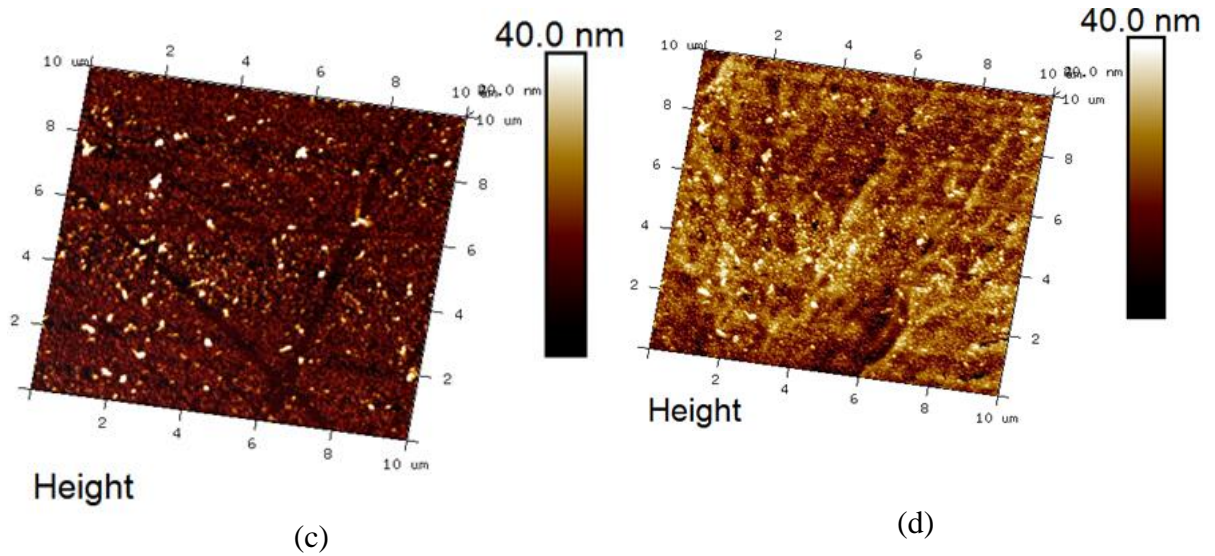


Fig. 23. FINEMET thin film with thickness of 50 nm a) 2D topography, b) 2D magnetic map, c) 3D topography in real scales, d) 3D phase MFM map overlaid on topography.

The 50 nm thick specimen was examined at 100 nm lift above the sample surface. The average surface roughness was 4.1 nm, and the RMS roughness was 5.8 nm. In addition to the presence of a multitude of small particles, 50 large particles with a height of 15 nm to 30 nm and a diameter of approximately 150 nm were found. Difference in contrast for domains of opposite orientation is 0.5° of phase shift in MFM, distinguishing domains with approximately 300 nm in width and several microns long.

The fourth type of FINEMET thin film was taken with thickness of 100 nm. An optical view of the scanned area is presented in Fig. 24.

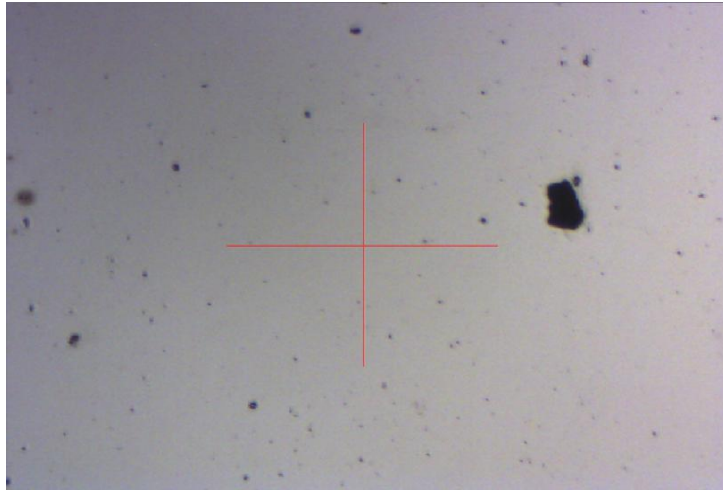
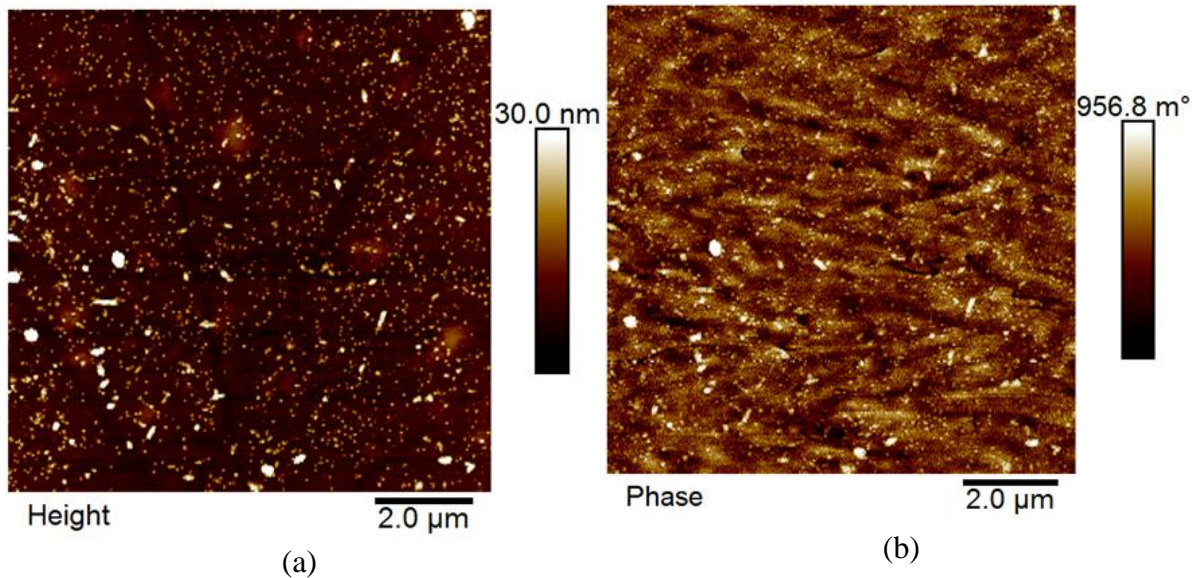


Fig.24. Optical view scanning area of FINEMET sample with thickness 100 nm.

The 100 nm thick thin film sample showed that the RMS roughness is 4.4 nm and the average roughness is 2.5 nm. The amount of particles in the $10\ \mu\text{m} \times 10\ \mu\text{m}$ scan was found to be approximately 1500. Also, the average height of particles is from 2 nm to 7 nm with the average diameters of particles approximately 80 - 100 nm. The magnetic map demonstrates the presence of magnetic domains with a contrast of oppositely oriented domains in $0.3^\circ - 0.4^\circ$ for some particles, but generally slightly more than 0.2° for the rest of particles in phase shift of the MFM. The difference in width between such domains turned out to be between 300 nm and 600 nm. Moreover, the presence of a stripe domain structure can be noted in fig. 25(b) that was not seen previously in the thinner samples.



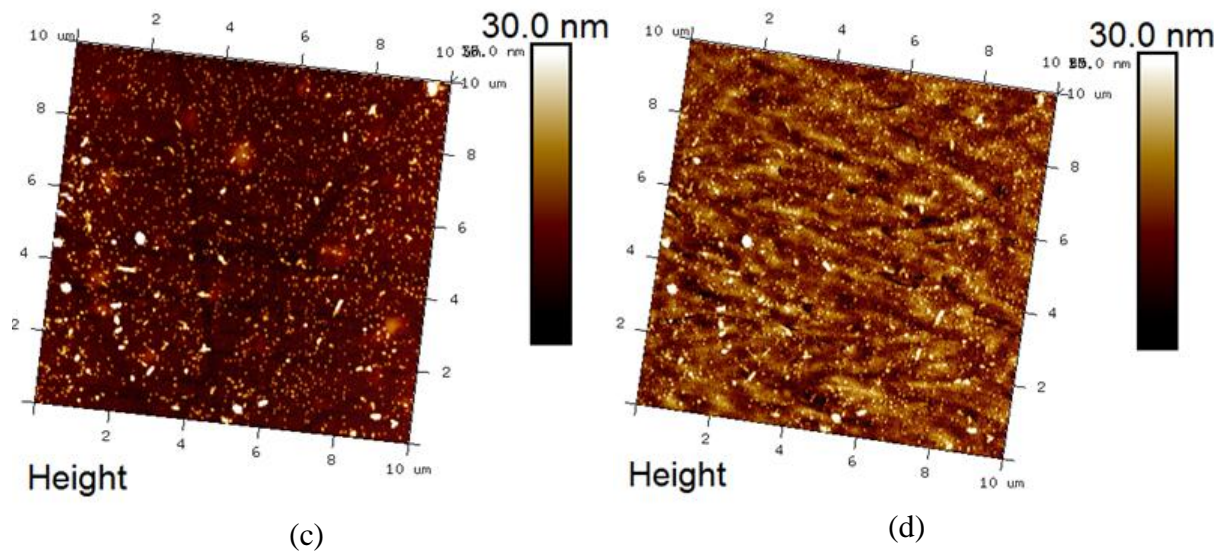


Fig. 25. FINEMET thin film with thickness of 100 nm a) 2D topography, b) 2D magnetic map, c) 3D topography in real scales, d) 3D phase MFM map overlaid on topography.

At some points of the sample surface, the film was detached from the substrate providing a place to check the real thickness of the sample. Figure 26 shows an optical image of the examined edge of the FINEMET film.

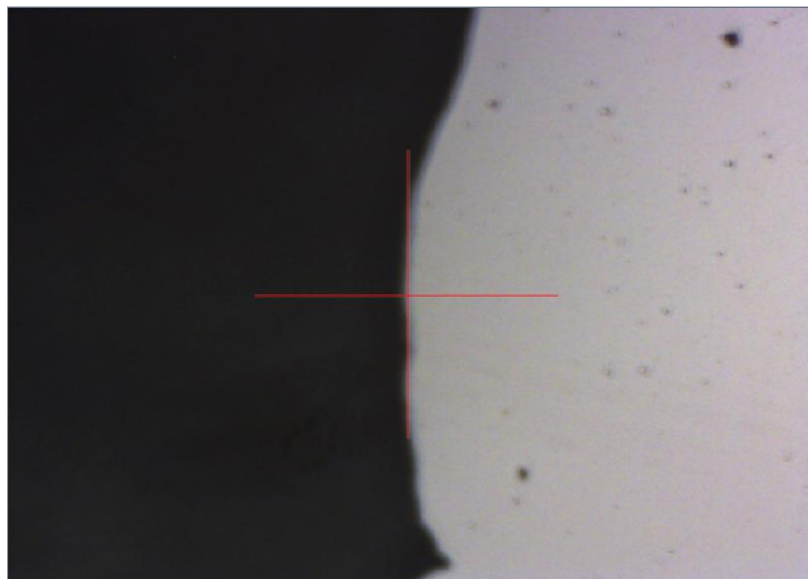


Fig.26. The scanning area of FINEMET sample for thickness detection.

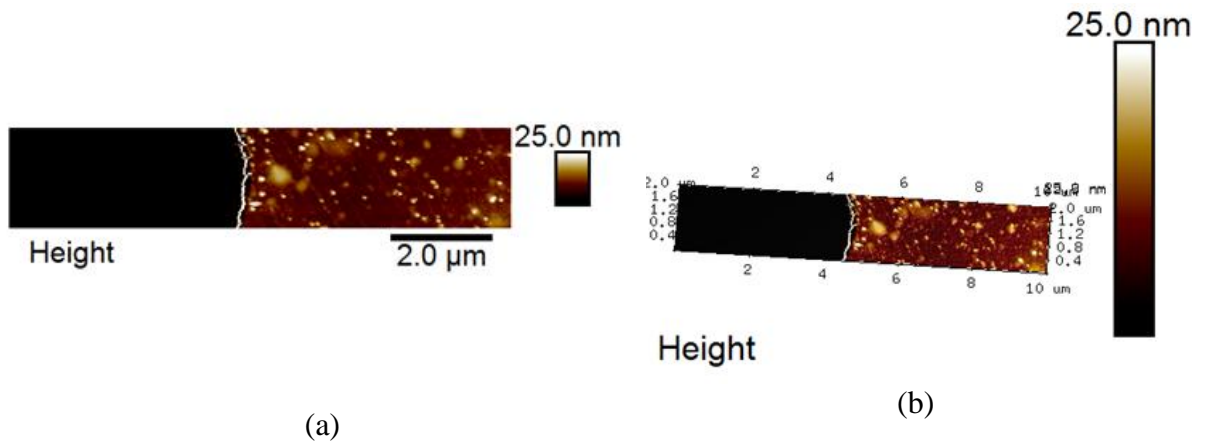


Fig.27. 2D (a) and 3D (b) dimensions of FINEMET thin film border with thickness 100 nm.

The data was processed using program NanoScope Analysis 1.8. Figures 27 (a) and (b) presents the film thickness in real scales. Figure 28 shows the profile view of height of the sample edge above the substrate.

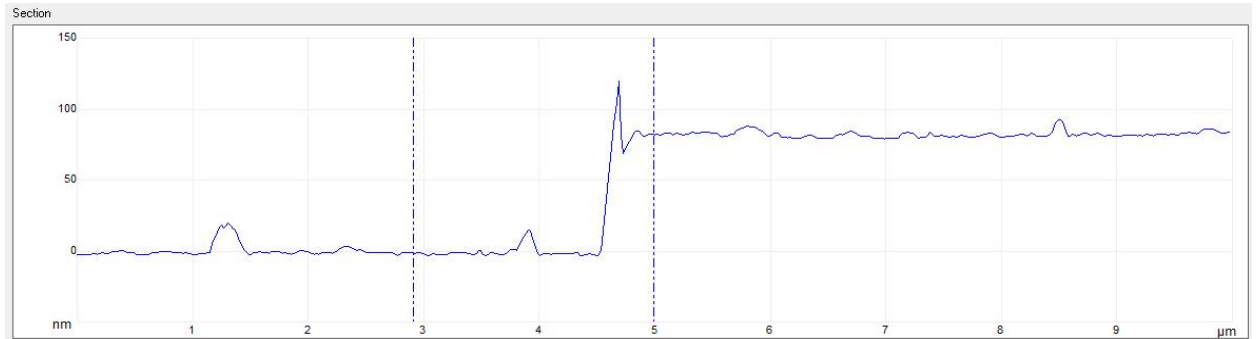


Fig. 28. The height of FINEMET thin film profile on the film edge.

During the experiment, it was observed that the actual film thickness was in average 83.5 nm, instead of 100 nm.

Table 1 presents the scope of experimental data for the four investigated samples with different thickness. The table shows values of roughness RMS, average roughness and lift of the probe for MFM.

Table 1. Properties of surface of studied samples

| | Thickness | Roughness RMS | Average roughness | Lift |
|---|-----------|---------------|-------------------|--------|
| Finemet thin film, annealed at 450°C for 30 minutes | 10 nm | 4.4 nm | 2.3 nm | 50 nm |
| | 30 nm | 6.9 nm | 5.4 nm | 70 nm |
| | 50 nm | 5.8 nm | 4.1 nm | 100 nm |
| | 100 nm | 4.4 nm | 2.5 nm | 100 nm |

It was found that the four investigated samples with different film thicknesses have in general the same roughness. This can be explained by the fact that the films were prepared by the same synthesis routine and the only changed parameter was the time of film deposition. However, the thinnest film had more of large particles with an average diameter of 300 nm on its surface. All the samples had scratches on the surface, which somehow are connected with the production technique, e.g. annealing processing.

The magnetic mapping of the samples surfaces showed different behavior between the samples of different thicknesses. The thin films with 10 nm and 30 nm thicknesses had the magnetic domains of 300 - 600 nm diameters. The domain size grew with the film thickness. Starting from the 50 nm film, the domains transformed into domain stripes 300 nm wide and several microns long. In case of the 100 nm (or ~85 nm, as found by AFM) film, the parameters of the domain stripes was the same but the density of stripes increased.

5.5 SQUID results of FINEMET alloys.

The study of the magnetic properties of the FINEMET alloys was made by investigating thin films with the help of various types of equipment. To obtain magnetic properties and dependencies, the studies were carried out using Superconducting Quantum Interference Device. SQUID has very high sensitivity, which can detect the presence of a weak magnetic field in the sample.

The basis for the formation of a super-high-density magnetic media comprise of the magnetic nanoparticles, which, due to exchange interactions, have a parallel orientation of their atomic moments. The magnetic moments are reoriented due to thermal energy coming from the environment, explicit temperature dependence arises [52-55]. Magnetic

characteristics of the samples measured using SQUID magnetometer are presented in this section in the form of temperature and magnetic field dependences of samples magnetizations.

The magnetization was measured in two configurations: parallel and perpendicular. The parallel configuration means that the external applied magnetic field is directed along the film plane. The orthogonal to that case is perpendicular configuration, where applied magnetic fields are directed perpendicular to the film plane. The magnetization data was compared to the results obtained by magnetic force microscopy. Therefore, samples with 30 nm, 100 nm, and 200 nm thick, were measured. The annealing effect was also studied by measuring an unprocessed sample and samples annealed at 400°C and 450°C. The investigations were carried out at different temperatures and magnetic field strengths at 5 Oe, 15 Oe, 30 Oe and 100 Oe.

The first sample was 200 nm thick annealed at 400 measured in parallel and perpendicular geometry. Its magnetic field dependences at temperature of 300 K are presented in Fig. 29. This sample shows the absence of a hysteresis loop, e.g. remanent magnetization and coercivity. The coercivity is less than 1 Oe. The comparison of results from the two geometries shows a presence of huge magnetic uniaxial anisotropy. The magnetization measured along the easy axis (parallel) saturates abruptly. It saturates to a 90% of saturation magnetization already at 12 Oe. However, the perpendicular magnetization was not saturated even at 1 T. At 1 T the magnetization value in the out-of-plane geometry reached around 25% of that in the parallel case.

In comparison to this sample, the sample of the same thickness, but annealed at 450°C showed the presence of hysteresis as can be seen in Fig. 30.

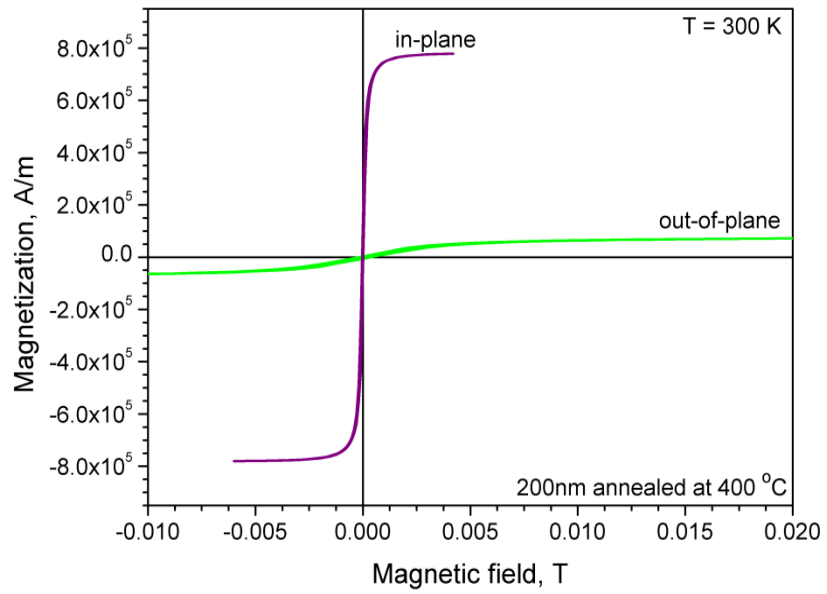


Fig. 29. The dependence of magnetization on magnetic field at $T= 300\text{K}$ in 200 nm thick and annealed at 400°C sample. The violet curve is parallel magnetization, whereas the green curve represents the perpendicular magnetization.

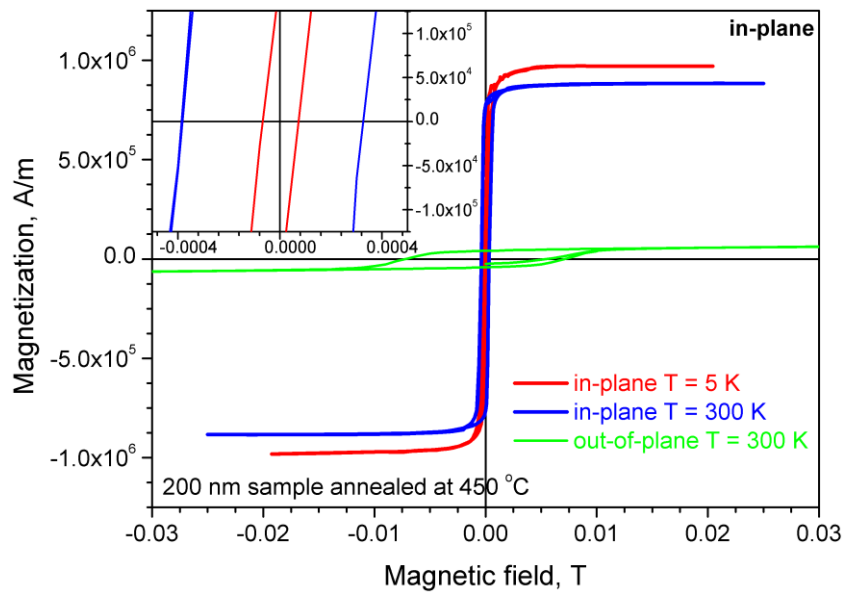


Fig. 30. The dependence of magnetization on magnetic field at $T= 300\text{K}$ in parallel (blue) and perpendicular (green) geometry. Also is shown $T= 5\text{K}$ (red) in parallel geometry. Measurements were done for 200 nm thick sample annealed at 450°C .

From fig. 30 it can be noted that at a temperature $T = 300$ K, the hysteresis loop in the parallel measurement became wider, than at the temperature $T = 5$ K for the same geometry. In addition to this, the coercivity turned out to be 0.8 Oe at 5 K and 4 Oe at 300 K. In the out-of-plane measurement at the temperature 300 K the coercivity was 80 Oe. It should be noted that the measurements were made at a magnetic field up to 1 T, but since the magnetization changed slowly, the data is presented in a field range from -0.03T to 0.03T. The saturation of magnetization was not reached due to the presence of strong uniaxial anisotropy. Hence, the deposition of films in external magnetic field induces very strong uniaxial anisotropy, which can be of high advantage in some applications.

Next, temperature dependences of magnetization of the samples 30 nm, 100 nm and 200 nm thick annealed at 450°C and without annealing were studied using different magnetic field strengths. The data was collected in the measurement range from 5 K to 350 K. Figure 31 shows the magnetic curves obtained as a result of the application of the magnetic field strength $H = 5$ Oe (Fig. 31 (a)), $H = 15$ Oe (Fig. 31 (b)), and $H = 30$ Oe (Fig. 31 (c)) for a sample of 100 nm thick annealed at 450°C. The sample was measured in zero-field-cooled (ZFC) protocol. This means that the sample was preliminarily cooled to a temperature of 5 K in a zero magnetic field. After reaching the highest temperature, the heated sample was slowly cooled down and upon returning back the data was registered. This sequence of procedures is called field-cooled (FC) protocol.

As can be seen from Figs. 31 (a)-(c), the temperature dependences show superparamagnetic behavior having a dome-like shape of the ZFC curve. The superparamagnetic behavior is due to the nature of the material. The film consists of nanoscale magnetic crystallites, which are in a blocking state at low temperatures. It should be noted that the largest value of the blocking temperature (T_B) was for the field of 5 Oe. Therefore, for a small magnetic field strength, domains need higher thermal energy in order to reorient and align in the applied field direction. When the measuring field was raised to 15 Oe, the blocking temperature was changed to a lower value by approximately 67 K. In this case the magnetic field was high enough to flip more spins than in case of lower field at the same temperature. Finally, at the applied magnetic field strength of 30 Oe, the differences between ZFC and FC curves were insignificant and no presence of clear blocking temperature was found. It should be noted that the field of 30 Oe is of the order of magnitude of saturation field.

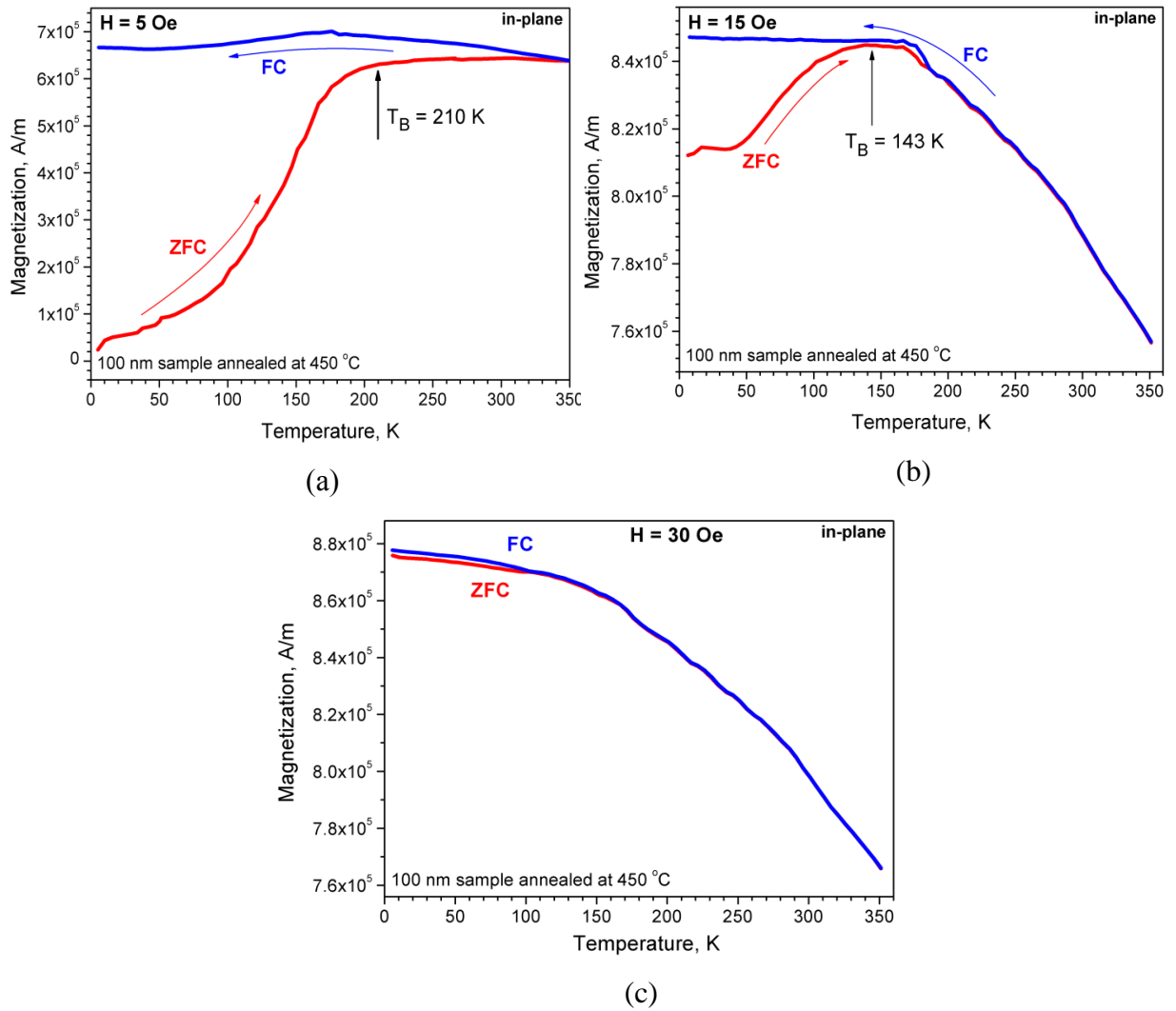


Fig. 31. The temperature dependences of ZFC and FC magnetization response for FINEMET film annealed at 450°C and 100 nm thick measured at $H = 5$ Oe (a), $H = 15$ Oe (b), and $H = 30$ Oe (c).

Figure 32 presents two graphs of the magnetization dependences on temperature at ZFC and FC for 200 nm thick samples annealed at 450°C (b) and 400°C (a). For a sample annealed at 450°C at 5 Oe field strength, the blocking temperature was $T_B=120$ K, while at a higher field strength ($H = 15$ Oe) for a sample annealed at 400°C, the blocking temperature was $T_B=157$ K.

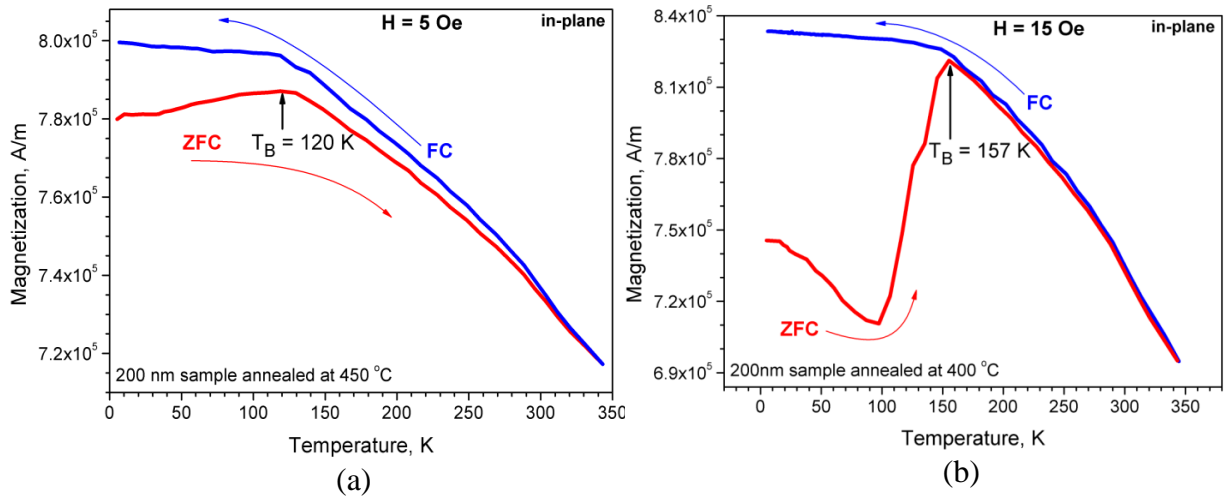


Fig. 32. The temperature-dependent ZFC and FC magnetization responses for 200 nm thick FINEMET films annealed at 450°C (a) and 400°C (b).

Moreover, a sharp jump in magnetization was observed with the temperature rising from 100 K to the blocking temperature in ZFC response in the Fig. 32(b). Although, for a sample annealed at 450°C the given jump is not present and the curve changes gradually with the increase of temperature (Fig. 32(a)).

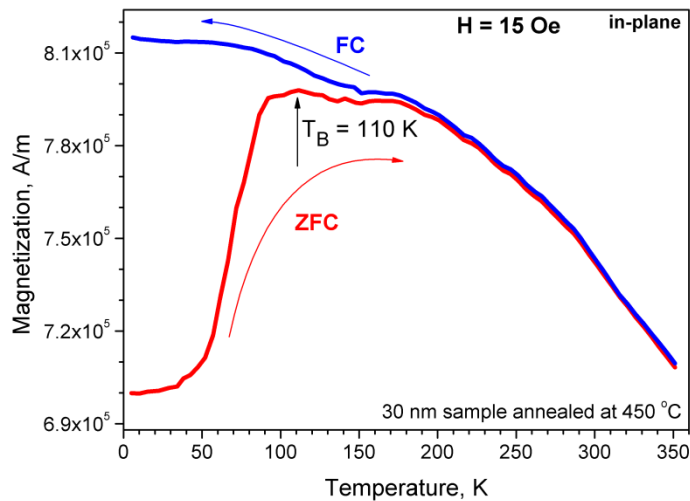


Fig. 33. The temperature-dependent ZFC and FC magnetization responses for FINEMET films 30 nm thick and annealed at 450°C in H=15 Oe field strength.

The study sample FINEMET thin film 30 nm thick annealed at 450°C placed in the

field strength $H = 15$ Oe is shown in Fig. 33. The blocking temperature occurred at $T_B=110$ K. There was a remarkable increase in magnetization at temperatures from 50 K to 110 K, when the sample was heated during the measurement from 5 K to 350 K. The sample changed its magnetization from $7 \cdot 10^5$ A/m to $8 \cdot 10^5$ A/m (ZFC red curve in Fig. 33). Such sharp increasing is a characteristic for a narrow distribution of magnetic fine particles.

An interesting aspect was found in studies of a sample without annealing with a thickness of 200 nm. Due to the increase in temperature values, its magnetization decreased (ZFC curve), and in the reverse path, during cooling, magnetization increased (FC curve), but the curves did not follow the same path. There was no blocking temperature observed in this sample. The data are shown in fig. 34.

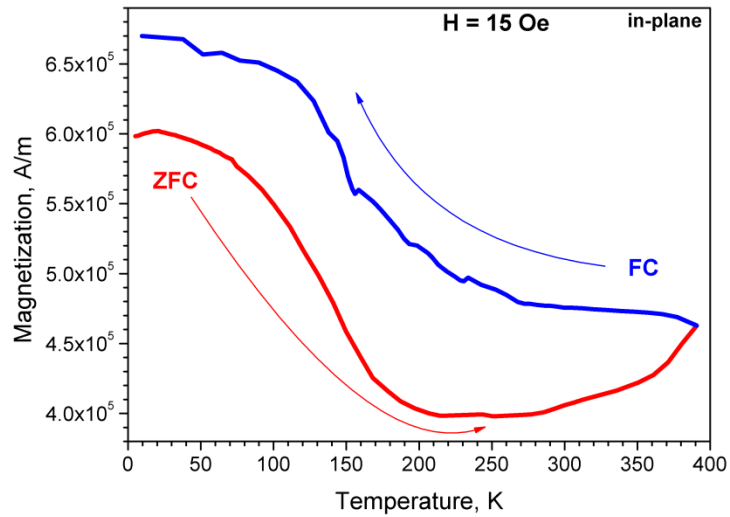


Fig. 34. The temperature-dependent ZFC and FC magnetization responses for as-cast FINEMET film 200 nm thick in $H=15$ Oe.

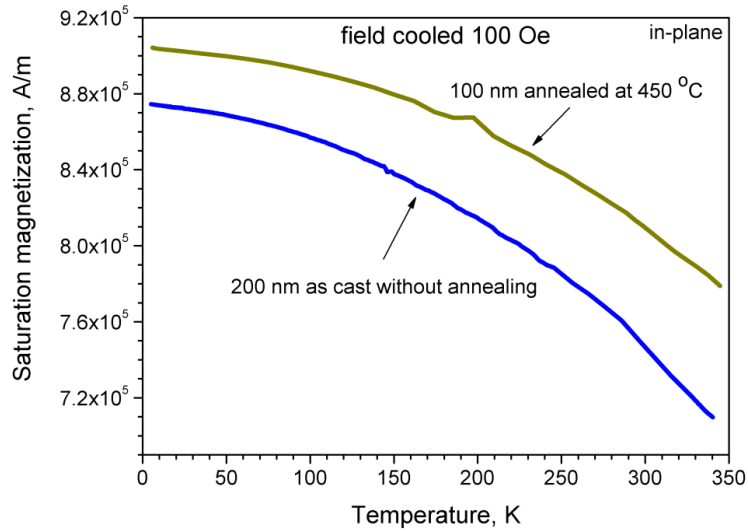


Fig. 35. The temperature dependence of saturation magnetization for as-cast 200 nm thick FINEMET film and 100 nm thick film annealed at 450°C in the field $H=100$ Oe.

Figure 35 presents two curves demonstrating two different samples in a strong field strength of $H = 100$ Oe. When the samples were cooled in the FC regime, their saturation magnetization increased gradually for both samples, as for the sample annealed at 450°C and 100 nm thick.

As a result of the magnetic investigation, the films showed very strong parallel uniaxial anisotropy, so that in the perpendicular geometry the saturation did not occur even at high field values. The samples saturated quickly at low fields in the parallel geometry. The coercivity was around 1 Oe, which is small and useful for applications. The low coercivity corresponds to low remagnetization losses. A slightly higher coercivity was found in the 200 nm thick sample annealed at 450°C. The temperature variations of magnetization had superparamagnetic behavior with blocking temperature. The blocking temperature varied with the strength of applied magnetic field. The temperature dependences of saturation magnetization had a ferromagnetic nature.

6 CONCLUSION

The main purpose of this thesis was to detect magnetic properties in FINEMET alloys. We used samples of different thicknesses from 10-200 nm, made without annealing and annealed at temperatures of 350°C, 400°C and 450°C.

The X-ray diffractometry revealed that all the films were amorphous. However, the FINEMET films annealed at 450°C had peak at 45°, which other samples did not have. This peak corresponds to Fe₃Si. Therefore, it is possible to make a conclusion that annealing at temperatures of 400°C and below does not lead to the formation of Fe₃Si crystallites. The average crystallite size of 17 nm was determined using the Scherrer's formula.

Raman spectroscopy showed a double peak in the range from 1300-1600 cm⁻¹. These peaks correspond to disordered defective graphite at 1300 cm⁻¹ and to polycrystalline graphite at 1600 cm⁻¹. The appearance of carbon traces has unknown nature.

The magnetic mapping of the samples surfaces obtained with MFM showed different behavior between the samples of different thicknesses. The thin films with 10 nm and 30 nm thicknesses had the magnetic domains of 300 - 600 nm diameters. The domain size grew with the film thickness. Starting from the 50 nm film, the domains transformed into domain stripes 300 nm wide and several microns long. In case of the 100 nm film, the parameters of the domain stripes were the same but the density of stripes increased. This behavior was observed also on the magnetization data of the samples. All the samples had strong uniaxial anisotropy. The anisotropy was induced by the parallel processing field of 100 Oe which was applied during the deposition process. The perpendicular magnetization did not saturate even at 1 T external field and reached only ~30% value of the saturate magnetization obtained in the in-plane geometry. The materials showed good soft magnetic properties with low coercivity and, hence, low magnetic losses.

In the MFM studies that were made by an AFM microscopy the significant domain structure was noticed on the magnetic map of the samples with higher annealing temperature.

However, despite the conducted studies, there is still room for further experiments for findings an important application of FINEMET samples for scientific purposes.

REFERENCES

1. Aliofkhazraei M. Size Dependency in Nanostructures. Nanocoatings, Springer Berlin Heidelberg, 2011, pp. 29-76.
2. Yoshizawa Y., Oguma S., Yamauchi K. New Fe-based soft magnetic alloys composed of ultrafine grain structure. Journal of Applied Physics, №. 10, T. 64, 1988, C.6044-6046.
3. Hono K. et al. The microstructure evolution of a Fe₇₃. 5Si₁₃. 5B₉Nb₃Cu₁ nanocrystalline soft magnetic material . Acta Metallurgica et Materialia, №. 9, T. 40, 1992, C. 2137-2147.
4. Maslov V. et al. Nanocrystallization in alloys of Finemet type. Phys Metals Metal Sci, T. 91, 2001, pp. 47-55.
5. Hono K. Nanoscale microstructural analysis of metallic materials by atom probe field ion microscopy. Progress in Materials Science, №. 6, T. 47, 2002, pp. 621-729.
6. Gercsi Z. Structural and thermal dependence of soft magnetic properties of FeCo-based nanocrystalline materials. Mechanics, Ecole normale sup_erieure de Cachan. ENS Cachan, 2004.
7. Song Q. Size and Shape Controlled Synthesis and Superparamagnetic Properties of Spinel Ferrites Nanocrystals : Dissertation. Georgia Institute of Technology, 2005.
8. Duwez P., Lin S. C. H. Amorphous ferromagnetic phase in iron-carbon-phosphorus alloys, 1967.
9. F. Fiorillo Soft magnetic materials. Wiley Encyclopedia of Electrical and Electronics Engineering., J. Webster (ed.), 1999, p. 23.
10. Nanocrystalline soft magnetic material FINEMET. Hitachi Metals, Ltd. brochure No. HL-FM10-C, 2005, pp. 2-4.
11. Starodubtsev Y., Belozarov V. Nanocrystalline soft magnetic materials. Journal Components & technologies, No.4, 2007.
12. Herzer G. Nanocrystalline Soft Magnetic Materials. Physica Scripta, T49, 1993, pp. 307-314.
13. Müller M., Mattern N. The influence of refractory element additions on the magnetic properties and on the crystallization behaviour of nanocrystalline soft magnetic Fe-B-Si-Cu alloys . Journal of Magnetism and Magnetic Materials, №. 1-2, T. 136, 1994, pp. 79-87.
14. Zencik, T., Jiraskova, Y., Zaveta, K., Eckert, D., Schneider, J., Mattern, N. and Hesse, D., Materials Letters 10, 313, 1991.

15. Herzer, G., Int. Symp. on 3rd Transition-Semi Metal Thin Films. Sendai Proceedings,, Japan, 1991, pp. 130, 307-314.
16. F. Pfeiffer and C. Radloff, J. Magn. Magn. Mat. 19,190, 1980.
17. MD. Sultan Mahmud Permeability and Hysteresis Loop Measurements of Amorphous and Annealed Samples of $Fe_{73.5-x}Cr_xCu_1Nb_3Si_{13.5}B_9.5$ Alloys. International Journal of Advanced Materials Science (ISSN 2231-1211), Vol. 4, No 2, 2013, pp. 141-147.
18. Colonel Wm.T. McLyman, Transformer and Inductor Design Handbook, 3rd edition, Marsel Dekker Inc., New York, 2004, 29, 532.
19. Cullity B. D., Graham C. D. Introduction to magnetic materials. Published by John Wiley & Sons, Inc., Hoboken, New Jersey, 2nd edition, 2011, p.361.
20. Mørup S. and Hansen M. F. Handbook of Magnetism and Advanced Magnetic Materials. John Wiley & Sons, edited by Kronmuller H. and Parkin S., Vol. 4, Chap. Superparamagnetic Particles, 2007.
21. Bean C. P., Livingston J. D. Superparamagnetism. Journal of Applied Physics, №. 4, T. 30, 1959.
22. Gengnagel, H. and Wagner, H., Z. angew. Physik 8,174, 1961.
23. Suzuki, K., Makino, A., Kataoka, N., Inoue, A. and Masumoto, T., J.Appl. Phys. Soft magnetic properties of nanocrystalline bcc Fe-Zr-B and Fe-M-B-Cu (M= transition metal) alloys with high saturation magnetization. Journal of Applied Physics, №. 10, T. 70, 1991, C. 6232-6237.
24. Bragg W.L. Proc. Cambridge Phil. Soc. 17, P.43. 1913.
25. Klopotov A.A., Abzaev Y.A., Potekayev A.I., Volokitin O.G. Basics of X-ray structural analysis in material science. Textbook, Publishing house – TGAUU, 2012, pp. 11-23.
26. Raman C.V. A new radiation, Ind. J. Phys.,V. 2, 1928, pp. 387-398.
27. Web site: http://www.nobelprize.org/nobel_prizes/physics/laureates/1930/index.html
28. Andrews, D. L. Applied Laser Spectroscopy. Weinheim: VCH Verlagsgesellschaft, 1992.
29. Schrader B. Infrared and Raman Spectroscopy. Weinheim: VCH, 1994.
30. Gardiner, D.J. Practical Raman spectroscopy. Springer-Verlag, 1989.
31. Sun S. and Murray C. B. Synthesis of monodisperse cobalt nanocrystals and their assembly into magnetic superlattices. Journal of Applied Physics, vol. 85, no. 8, 1999, pp. 4325–4330.
32. Binnig G. and Rohrer H., Helv. Phys. Acta, 55, 726, 1982.
33. Binnig G., Quate C. F. , Gerber Ch . Atomic Force Microscope. PRL 9, 56, 1986.

34. Barash Y. Van der Waals force. *Science*, 1988, p. 344.
35. Mironov V. The basis of Scanning Probe Microscopy. N. Novgorod, 2004, p. 114.
36. Hendrych A., Kubínek R., Zhukov A. V. The magnetic force microscopy and its capability for nanomagnetic studies-The short compendium. *Modern Research and Educational Topics in Microscopy*, T. 2, 2007, C. 805-811.
37. Clarke J. SQUIDS: Theory and Practice. *The New Superconducting Electronics*, Kluwer Academic H. Weinstock, R. Ralston Eds, Dordrecht, 1993, p. 123.
38. Jaklevic R.C., Lambe J., Silver A.H., Mercereau J.E., *Phys. Rev. Lett.* 1964, 159, p.12.
39. London F. *Superfluids*. Vol. 1, Wiley, New York, 1950.
40. Josephson B. D. Possible new effects in superconductive tunneling. *Phys. Lett.* V. 1., 1961, pp. 251–253.
41. Anderson, P., Rowell, J. Probable Observation of the Josephson Superconducting Tunneling Effect. *Physical Review Letters*. 10 (6), 1963, pp. 230-232.
42. Clarke J. and Braginski A. I. *The SQUID handbook*. Vol. 1, Wiley-Vch, 2004.
43. Clarke J. SQUIDS. *Scientific American* 271, №2, August 1994, p 46.
44. Kornev V.K. The Josephson effect and its application in superconductor electronics. *Soros Educational Journal*, No. 8, 2001, p. 83.
45. User Manual: S700X SQUID Magnetometer, 17th January 2017, 161, p.10.
46. Sun S. and Murray C. B. Synthesis of monodisperse cobalt nanocrystals and their assembly into magnetic superlattices. *Journal of Applied Physics*, vol. 85, no. 8, 1999, pp. 4325–4330.
47. Scherrer P. Bestimmung der Gröss Kolloidteilchen Mittels Nachrichten von der Gesellschaft der Wissenschaften, Göttingen Mathematisch-Physikalische Klasse, Vol. 2, 1918, pp. 98-100.
48. Champion Y., Hans-Jorg Fecht, *Nano-architected and nanostructured materials. The fabrication, control and properties*. Weinheim : Wiley-VCH Verlag, 2005, p 90.
49. Langford J. and Wilson A. Scherrer after Sixty Years: A Survey and Some New Results in the Determination of Crystallite Size. *Journal of Applied Crystallography*, Vol. 11, 1978, pp. 102-103.
50. Web site: <https://www.xos.com/XRD>
51. Web site: <http://www.brukerafmprobes.com/p-3605-mesp-rc.aspx>
52. INTERTECH Corporation. Introduction to Raman spectroscopy. *Plastic masses*. No. 8, 2009, pp. 7-13.
53. Reiss G. and Hütten A. Magnetic nanoparticles: applications beyond data storage. *Nature*

Materials, vol. 4, no. 10, 2005, pp. 725–726.

54. Frey N. A. and Sun S. Magnetic nanoparticle for information storage applications in *Inorganic Nanoparticles: Synthesis, Applications, and Perspectives*. CRC Press, New York, NY, USA, C. Altavilla and E. Ciliberto, Eds., chapter 3, 2010, pp. 33–68.
55. Lewin W. Hook's Law, Simple Harmonic Oscillator, 1999.